



Karasaki, T. et al. (2023) Evolutionary characterization of lung adenocarcinoma morphology in TRACERx. *Nature Medicine*, 29(4), pp. 833-845.

There may be differences between this version and the published version. You are advised to consult the publisher's version if you wish to cite from it.

<https://eprints.gla.ac.uk/297218/>

Deposited on: 26 April 2023

Enlighten – Research publications by members of the University of Glasgow
<https://eprints.gla.ac.uk>

Evolutionary characterization of lung adenocarcinoma morphology in TRACERx

Received: 26 April 2022

Accepted: 24 January 2023



 Check for updates

A list of authors and their affiliations appears at the end of the paper

Lung adenocarcinomas (LUADs) display a broad histological spectrum from low-grade lepidic tumors through to mid-grade acinar and papillary and high-grade solid, cribriform and micropapillary tumors. How morphology reflects tumor evolution and disease progression is poorly understood. Whole-exome sequencing data generated from 805 primary tumor regions and 121 paired metastatic tumors across 248 LUADs from the TRACERx 421 cohort, together with RNA-sequencing data from 463 primary tumor regions, were integrated with detailed whole-tumor and regional histopathological analysis. Tumors with predominantly high-grade patterns showed increased chromosomal complexity, with higher burden of loss of heterozygosity and subclonal somatic copy number alterations. Individual regions in predominantly high-grade pattern tumors exhibited higher proliferation and lower clonal diversity, potentially reflecting larger recent subclonal expansions. Co-occurrence of truncal loss/loss of heterozygosity of chromosome 3p and 3q was enriched in predominantly low-/mid-grade tumors, while purely undifferentiated solid-pattern tumors had a higher frequency of truncal arm or focal 3q gains and *SMARCA4* gene alterations compared to mixed-pattern tumors with a solid component, suggesting distinct evolutionary trajectories. Clonal evolution analysis revealed that tumors tend to evolve toward higher-grade patterns. The presence of micropapillary pattern and ‘spread through air spaces’ were associated with intrathoracic-only recurrence, in contrast to the presence of solid/cribriform patterns, necrosis and preoperative circulating tumor DNA detection, which were associated with extra-thoracic recurrence. These data provide insights into the relationship between LUAD morphology, the underlying evolutionary genomic landscape, and clinical and anatomical relapse risk.

Q1
Q2 Lung cancer, the leading cause of cancer-related death globally, encompasses a range of different histological entities. LUAD, the commonest histology, is a morphologically and genetically diverse disease with various histological features relating to tumor behavior. This includes

the range of tissue architectural growth patterns from ‘lepidic’, which is well differentiated and noninvasive, through to undifferentiated ‘solid’¹, as well as mucinous differentiation observed in invasive mucinous adenocarcinoma (IMA)² (Extended Data Fig. 1a–h), and the presence

of ‘spread through air spaces’ (STAS)³. Growth patterns, categorized as lepidic (low grade), papillary and acinar (mid grade) and cribriform, micropapillary and solid (high grade), are frequently combined within a single LUAD tumor, and the proportion of high-grade patterns within each tumor is known to impact patient outcome⁴.

Previous genomic analysis of single tumor regions has shown that high-grade tumors harbor increased tumor mutational burden (TMB) and increased rates of whole-genome doubling⁵. Frequencies of somatic alterations in specific genes, such as *TP53*, together with the fraction of the genome altered by somatic copy number alterations (SCNAs), have been found to be increased in tumors with predominantly high-grade morphological patterns⁵. In a previous study of ten LUADs with microdissected multiregional omics data, differences in transcriptomic profiles, rather than genomic alterations, were more strongly associated with a shift between growth patterns⁶. However, the biological implications of different growth patterns, and their potential genomic underpinnings, remain poorly understood. We hypothesized that multiregional tumor sampling data from the TRACERx (TRACKing non-small cell lung Cancer Evolution through therapy (Rx)) cohort may elucidate how evolutionary progression determines histological LUAD subtypes. In particular, the presence of distinct growth patterns within individual tumors provides a natural experiment to explore how evolutionary genomic features relate to specific growth patterns while controlling for background clinical and germline features.

TRACERx is a prospective observational study of non-small cell lung cancer (NSCLC) from diagnosis through to cure or relapse, with multiregional primary and metastatic tumor sampling alongside longitudinal circulating tumor DNA (ctDNA) analysis and detailed clinical annotation, including patient outcome data^{7,8}. The TRACERx 421 cohort represents the first 421 patients prospectively recruited into the study^{9,10}. This includes 248 primary LUADs (805 tumor regions) from 242 patients, plus 121 paired metastatic lymph nodes (LNs) and recurrence tumors from 65 patients (Extended Data Fig. 1i,j). RNA-sequencing (RNA-seq) data were available for 189 of these primary tumors (463 tumor regions)¹¹. Here we describe the molecular characteristics of LUAD evolution and progression with respect to tumor morphology using multiregional whole-exome sequencing (WES) and transcriptomic data.

Results

Clonal evolutionary characteristics of LUAD growth patterns

To elucidate the characteristics of each growth pattern in LUAD, clinical, pathological and genomic features across the different predominant subtypes at the whole-tumor level were analyzed (Fig. 1a, Extended Data Fig. 1k,l and Supplementary Tables 1–3). The proportion of high-grade patterns (solid, cribriform and micropapillary) within a tumor, based on sectional area in the diagnostic H&E-stained slides at the whole-tumor level, was assessed in the context of variables associated with subclonal architecture and genomic instability (Fig. 1b and Methods). An increased proportion of high-grade patterns at the whole-tumor level was associated with higher truncal, but not subclonal, TMB (truncal TMB, Spearman’s $\rho = 0.25$, q value (false discovery rate (FDR)-adjusted P value) = 0.0011, subclonal TMB, $\rho = 0.12$, $q = 0.11$). Features of chromosomal complexity and instability, including the mean weighted genome instability index (wGII), mean fraction of the genome subject to loss of heterozygosity (FLOH) and the SCNA intra-tumoral heterogeneity (ITH) score^{7,8} (a percentage of subclonal SCNAs), were significantly associated with the proportion of high-grade patterns within a tumor (wGII, $\rho = 0.15$, $q = 0.040$; FLOH, $\rho = 0.35$, $q = 2.6 \times 10^{-6}$, percentage subclonal SCNA, $\rho = 0.32$, $q = 1.3 \times 10^{-5}$, Methods and Fig. 1b). Similar results were observed when using an orthogonal tool for SCNA analysis (Sequenza)¹² and an orthogonal method for calling mutational clonality (Extended Data Fig. 2a–c and Methods).

In our companion paper⁹, we found that the presence of large recent subclonal expansion in primary tumor regions was associated

with shorter disease-free survival (DFS)^{9,10}. In LUAD, metrics capturing the presence of a recent subclonal expansion and associated mutational homogeneity within individual tumor regions were significantly associated with an increased proportion of high-grade patterns (Fig. 1b). These metrics included the number of subclonal mutations, which were clonal in at least one region ($\rho = 0.20$, $q = 0.0087$) and the recent subclonal expansion score⁹, defined as the largest cancer cell fraction (CCF) of any subclone terminal to the phylogenetic tree in any tumor region ($\rho = 0.14$, $q = 0.049$; Methods). Conversely, the subclonal diversity index, a metric reflective of the number of coexisting subclones in a region and the absence of large recent clonal expansions, was significantly lower in those tumors with a higher proportion of high-grade patterns (minimum subclonal diversity per tumor, $\rho = -0.22$, $q = 0.0031$; Methods). Ki-67 fraction was significantly associated with an increasing proportion of high-grade patterns ($\rho = 0.51$, $q = 1.4 \times 10^{-11}$), consistent with previous reports^{6,13}. Taken together, these data suggest that while different regions from a high-grade tumor are genomically distinct and can harbor region-specific SCNAs, individual regions tend to be highly proliferative and clonally pure, potentially reflective of large intra-regional recent subclonal expansions.

When the proportion of each individual growth pattern was compared with these genomic features, high proliferation and the presence of recent subclonal expansion was most strongly associated with the proportion of solid-pattern component within a tumor (Ki-67 fraction, $\rho = 0.51$, $q = 7.3 \times 10^{-11}$, recent subclonal expansion score, $\rho = 0.17$, $q = 0.036$; Fig. 1c). Intriguingly, although micropapillary pattern is regarded as a high-grade pattern associated with poor prognosis¹⁴, in TRACERx LUADs an increasing proportion of micropapillary pattern component was associated with increasing subclonal diversity and a lack of evidence for clear subclonal expansions (minimum subclonal diversity per tumor, $\rho = 0.22$, $q = 0.0078$, recent subclonal expansion score, $\rho = -0.19$, $q = 0.027$), suggesting distinct biology and clonal evolutionary characteristics between high-grade solid and micropapillary growth patterns.

Genomic determinants of predominant growth pattern

To explore the evolutionary determinants of growth patterns in LUAD, truncal genomic alterations were correlated with the predominant pattern within a tumor, assuming that specific early genomic events may influence the subsequent growth pattern. In total, 8 truncal driver alterations (6 mutations, 2 amplifications), 31 chromosomal arm-level truncal SCNAs (8 gains and 23 losses/LOHs) observed in at least 5% of the cohort were included in a logistic regression analysis (Extended Data Fig. 3a–c and Methods). Previous studies have reported an increased frequency of *TP53* (refs. 5,14,15) and *KRAS* (ref. 16) mutations in solid-predominant tumors. Here, in addition to truncal *TP53* and *KRAS* driver mutations, truncal *SMARCA4* mutation and truncal loss/LOH of chromosome 21q and 22q were associated with predominantly high-grade tumors, while truncal gains of 1q and 8q were associated with predominantly low-/mid-grade tumors (Fig. 2a). Similar results were observed when restricted to truncal alterations in at least 10% of the cohort, when applying an orthogonal tool (Sequenza)¹² for SCNA profiling, or when adding genomic instability as a covariate in the regression model (Extended Data Fig. 2d–f and Methods).

Co-occurrence of truncal loss/LOH of 3p and 3q was significantly overrepresented in predominantly low-/mid-grade tumors ($q = 0.0027$), but not in predominantly high-grade tumors (Fig. 2b, Extended Data Fig. 2g,h and Methods). Co-occurrence of truncal 3p and 3q loss/LOH within predominantly low-/mid-grade tumors was not associated with higher wGII, suggesting that co-occurrence of the loss of these chromosome arms does not reflect genomic instability ($P = 0.71$, Wilcoxon rank-sum test; Extended Data Fig. 2i). These results suggest that a co-occurrence of 3p and 3q loss, possibly reflecting the loss of one allele of whole chromosome 3 as a single event, is a distinct evolutionary route to predominantly low-/mid-grade tumors.

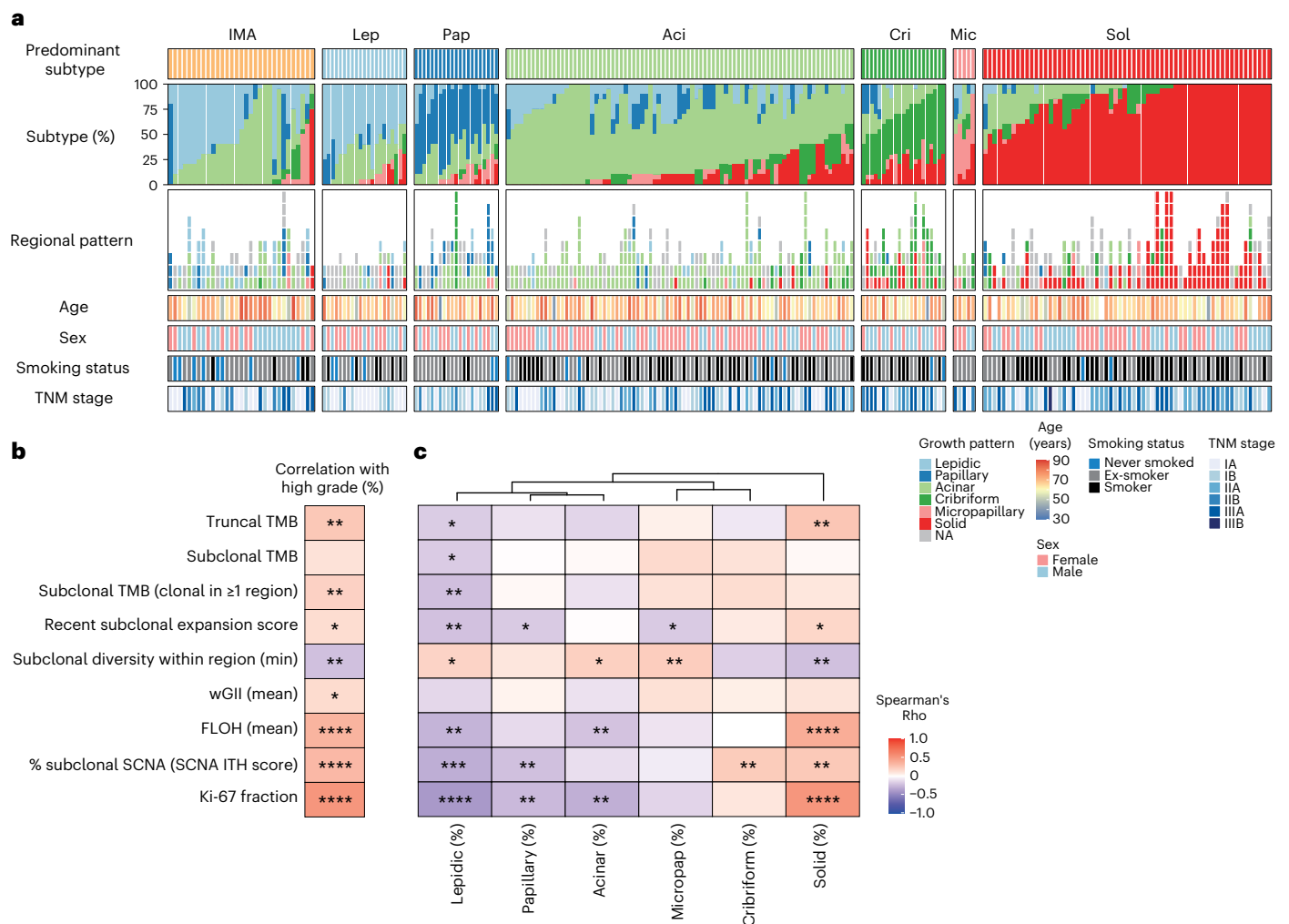


Fig. 1 | Clonal evolutionary characteristics of LUAD growth patterns.

a, Overview of TRACERx 421 LUAD cohort. Each column represents one tumor. Fetal adenocarcinoma, colloid adenocarcinoma and two tumors from a collision tumor determined by genomic analysis were not included in the plot ($n = 244$ tumors in 240 participants are shown). The proportion of each growth pattern based on diagnostic sectional area, the growth pattern for each region and basic

clinical information are summarized. **b, c**, Correlation of genomic variables and proportion of high-grade patterns (**b**) and proportion of each growth pattern (**c**) within each tumor. Color scale reflects Spearman's rank correlation coefficient (ρ). Correlation P values were corrected for multiple testing according to the Benjamini–Hochberg (BH) method. The asterisks indicate q values; * $q < 0.05$, ** $q < 0.01$, *** $q < 0.001$, **** $q < 0.0001$. NA, not applicable.

To evaluate SCNAs with $<5\%$ frequency in the cohort, which were excluded from the regression analysis, an analysis of the driver alterations and chromosomal arm-level copy number alterations varying between predominantly high-grade and low-/mid-grade tumors was carried out (Methods). The characteristics most strongly associated with predominantly high-grade tumors versus predominantly low-/mid-grade tumors were gains of chromosome arms 3q (encompassing the *SOX2* and *TERC* genes) and 12p (encompassing the *KRAS* gene, consistent with a previous report⁵; Fig. 2c and Extended Data Fig. 3d). Similar results were observed when applying an orthogonal tool (Sequenza)¹² for SCNA profiling, or when including genomic instability as a covariate in the regression model (Extended Data Fig. 2j,k and Methods).

At the transcriptome level, the greatest differential expression between high-grade and low-/mid-grade predominant tumors involved genes related to cell proliferation (Fig. 2d and Methods). Notably, predominantly high-grade tumors did not necessarily harbor increased copy number of proliferation pathway genes compared with predominantly low-/mid-grade tumors ($P = 0.36$, Chi-square test; Extended Data Fig. 3e and Methods), suggesting that the overexpression of these

genes in predominantly high-grade tumors may not be directly driven by copy number gains.

Cancer cell programmed death-ligand 1 (PD-L1) expression, assessed by immunohistochemistry, was significantly higher in solid-predominant tumors than all other histological subtypes ($q = 2.1 \times 10^{-7}$ Wilcoxon rank-sum test; Extended Data Fig. 3f), as previously reported¹⁴. The proportion of solid-pattern remained significantly associated with cancer cell expression of PD-L1 after adjustment for stromal tumor-infiltrating lymphocytes (TILs) and neoantigen burden (odds ratio (OR) = 1.23, 95% confidence interval (CI) 1.11–1.38, per 10% increase, $P = 3.8 \times 10^{-5}$, analysis of variance (ANOVA); Methods and Extended Data Fig. 3g), suggesting that overexpression of PD-L1 in solid-predominant tumors may be driven by cancer cell-intrinsic characteristics, such as AKT–mTOR pathway activation¹⁷.

Morphological intra-tumoral heterogeneity reflects genomic intra-tumoral heterogeneity

The data thus far focus on growth pattern characterization at the whole-tumor level. However, multiregional sampling and sequencing in TRACERx allows for the analysis of intra-tumoral growth pattern

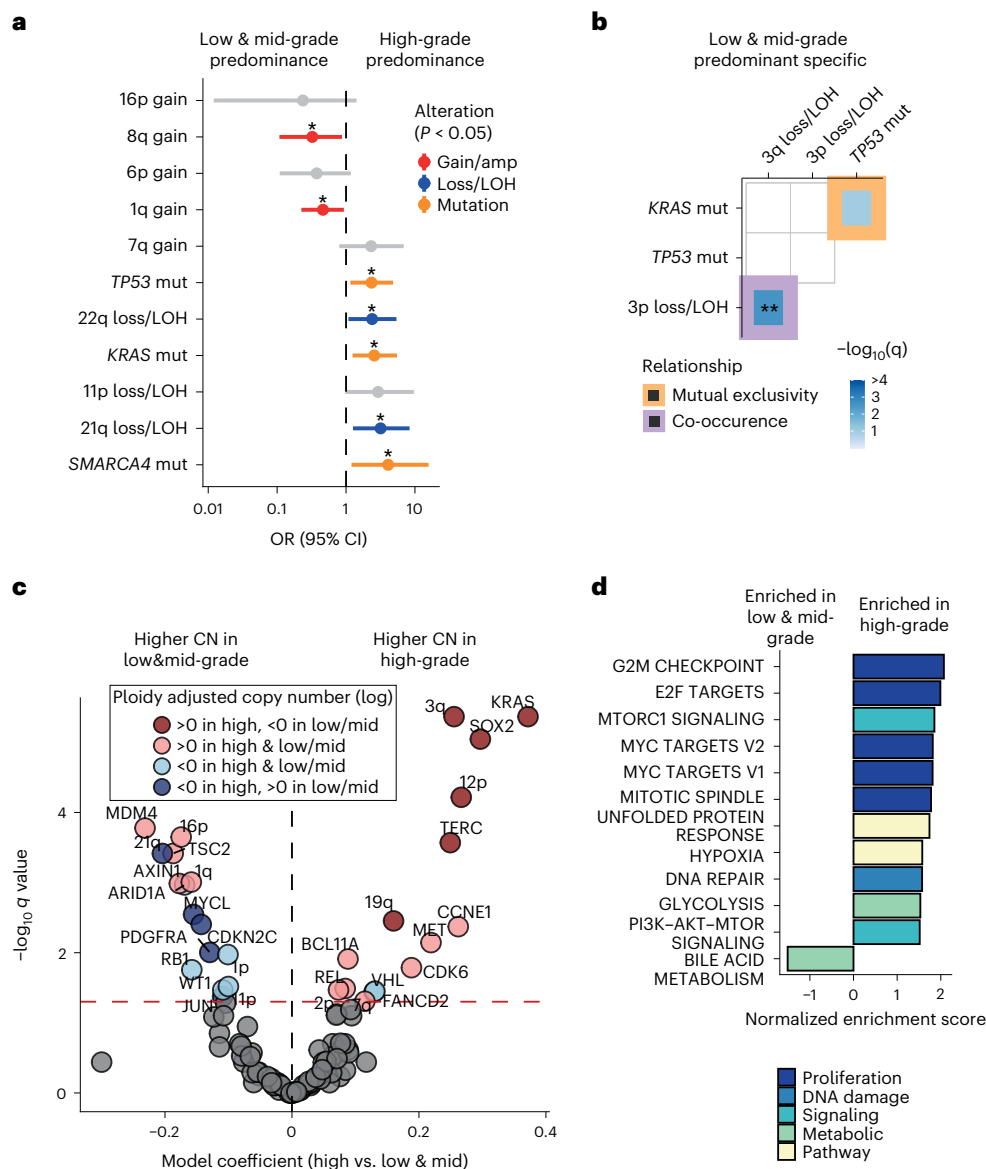


Fig. 2 | Genomic determinants of predominant growth pattern.

a, Adjusted ORs and 95% CIs of truncal genomic alterations associated with the predominantly high-grade pattern tumors ($n = 79$) compared with predominantly low-/mid-grade pattern tumors ($n = 116$). Genomic alterations selected by the model simplification are shown. Asterisks indicate statistically significant ($P < 0.05$) alterations. The ORs and P values were derived from single multivariable logistic regression analysis. Asterisks indicate type II ANOVA P values; * $P < 0.05$, ** $P < 0.01$, *** $P < 0.001$. Color represents the type of genomic alteration. **b**, Mutual exclusivity and co-occurrence of truncal driver gene mutations and chromosome arm SCNAs specific to predominantly low-/mid-grade tumors ($n = 116$). Color of the edge represents the relationship (mutual exclusivity versus co-occurrence). The negative log of the q value (BH method) is represented in the color scale within each tile. Relationships with $q < 0.1$

are shown, with statistically significant ($q < 0.05$) alterations indicated by the asterisks; * $q < 0.05$, ** $q < 0.01$. **c**, Comparison of ploidy-adjusted mean copy number of chromosomal arm and driver genes between high-grade and low-/mid-grade predominant tumors. Fixed-effect coefficients of the linear mixed-effect model with tumor as a random effect are displayed on the x axis, and the negative log of the q value (BH method) is displayed on the y axis. Color represents the sign of the mean ploidy-adjusted copy number, stratified with predominance of high-grade and low-grade/mid-grade patterns. Data points with q value ≥ 0.05 are colored gray. The horizontal red dashed line represents $q = 0.05$. **d**, Gene-set enrichment analysis of Hallmark gene sets between predominantly high-grade and low-grade/mid-grade tumors. The normalized enrichment score is displayed on the x axis and indicates the enrichment for a given gene set. Color represents the category of gene sets. Gene sets with $q < 0.25$ (BH method) are shown.

heterogeneity in the context of the genomic and transcriptomic landscape. A total of 200 tumors had available regional histology, amounting to 603 regions for analysis (Fig. 1a, Extended Data Fig. 1j,k and Supplementary Table 4).

Genomic distances based on mutations (single-nucleotide variants and indels) and LOH were calculated between regions of the same tumor and explored in relation to regional growth patterns, to determine whether variation in morphology is recapitulated in genomic space (Fig. 3a and Methods). The genomic distance between regions with

different growth patterns was significantly greater than the genomic distance between regions with the same growth pattern when calculated using LOH ($P = 0.0071$, linear mixed-effects model ANOVA; Methods), but not when using mutations ($P = 0.11$; Fig. 3b and Extended Data Fig. 4a–c). This may reflect that LOH is irreversible, whereas truncal mutations may be subject to copy number loss, making them appear as subclonal and potentially less reliable as a marker of evolutionary divergence.

To assess whether different morphological patterns reflect an evolutionary trajectory from low-grade to high-grade pattern, we utilized

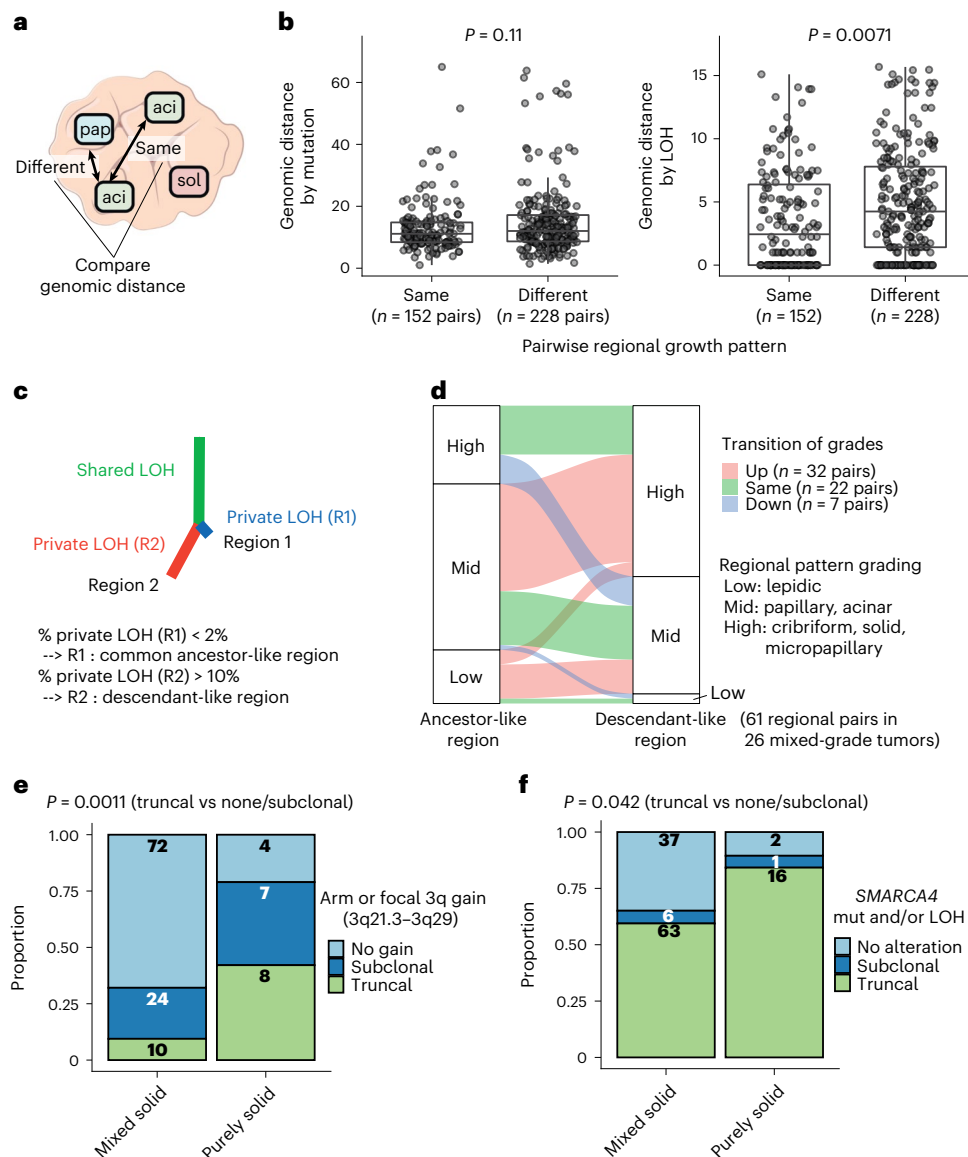


Fig. 3 | Morphological intra-tumoral heterogeneity reflects genomic heterogeneity.

a, Schematic illustrating regions with different or the same growth patterns within each tumor. **b**, Genomic distance between regions calculated by presence of somatic mutations and LOH. Genomic distances between pairs of identical (same) growth pattern regions and different growth pattern regions were compared. Each point represents a distance between a pair of regions in a tumor, and the number of regional pairs is shown under each group. 53 tumors containing regions with both different growth pattern pair(s) and same growth pattern pair(s) were included in the analysis. The center line is the median, box limits represent upper and lower quartiles, and whiskers represent 1.5 times the interquartile range. *P* values were calculated using a linear mixed-effects model, with tumor as a random effect. **c**, Schematic illustrating inference of ancestor-like and descendant-like regional pairs using shared and private LOH profiles per cytoband. After building an LOH tree, if a proportion of branch length of region 1 (R1) is shorter than 2%, namely if the number of private

LOH is less than 2% of the total number of LOH (shared + private) in R1, then R1 is inferred as a common ancestor-like region. Conversely, if a proportion of branch length of region 2 (R2) is longer than 10%, namely if the number of private LOH is greater than 10% of the total number of LOH in R2, then R2 is inferred as a descendant-like region. **d**, Comparison of growth pattern (grade) between inferred ancestor-like and descendant-like regions. Only tumors with mixed-pattern grades are presented. Color represents the transition of grade from ancestor-like to descendant-like regions. Enrichment of the transition from lower grade to higher grade (upward transition) was evaluated using a permutation test (1,000 permutations, randomizing growth patterns within each tumor, Monte-Carlo procedure). **e**, **f**, Comparison of the frequency of (e) truncal gain of chromosome arm or focal 3q (3q21.3–3q29) (**e**) and truncal *SMARCA4* mutation and/or LOH (**f**) between mixed-pattern tumors with solid component and purely solid tumors. A two-sided Fisher's exact test was used.

the irreversible nature of LOH to determine ancestor–descendant-like relationships between tumor regions within the context of their respective morphological grades (Fig. 3c and Methods). This was based on the assumption that, although a tumor region may not be directly evolved from another region, in some regional pairs one region will harbor a common ancestral-like clone, while the other region may harbor a descendant-like clone of the common ancestor. We identified 151

regional pairs with ancestor–descendant-like relationships within 54 tumors using LOH profiles. Comparison of the mutational profiles of these ancestor–descendant-like pairs revealed that descendant-like regions harbored additional mutations at a high CCF ($\geq 95\%$) compared to their ancestor-like counterpart regions ($P < 0.001$, permutation test; Methods and Extended Data Fig. 4d). Descendant-like regions exhibited a significantly higher grade compared with their respective

ancestral-like regions ($P = 0.005$, permutation test; Methods, Fig. 3d and Extended Data Fig. 4e). This association remained significant when different cutoffs were applied to infer ancestor–descendant-like regional pairs (Extended Data Fig. 4f), or when using an orthogonal tool (Sequenza)¹² for LOH profiling (Extended Data Fig. 4g). This association also remained significant when ancestor–descendant-like regional pairs were inferred using a combination of LOH and mutational profiles (Extended Data Fig. 4h and Methods). Notably, LUADs did not always follow an evolutionary route toward higher-grade patterns, suggesting that, although rare (7/151 ancestor–descendant-like regional pairs), it is conceivable that tumors may transition to lower-grade patterns during subclonal evolution (Extended Data Fig. 4e). Overall, these data suggest that heterogeneity in morphological patterns may be partially underpinned by genomic alterations, especially by subclonal LOH.

Distinct evolutionary trajectory of purely solid tumors

Tumors lacking any adenocarcinoma architectural differentiation, namely purely solid-pattern tumors, are typically classified as LUADs based on immunohistochemical expression of thyroid transcription factor (TTF)-1 alone. Molecular and evolutionary characteristics of purely solid tumors are poorly understood. In particular, whether purely solid tumors have evolved from mixed-pattern adenocarcinomas that include a solid component remains unclear. To address this, we explored whether solid-pattern regions in purely solid tumors and solid-pattern regions in mixed-pattern tumors harbored similar genomic and transcriptomic features, and if purely solid tumors were genomically distinct from mixed-pattern tumors with a solid component (mixed solid).

Solid regions in purely solid tumors showed overexpression of G2M checkpoint genes compared with solid regions in mixed growth pattern tumors ($P = 0.0026$, linear mixed-effect model, ANOVA; Extended Data Fig. 5a). At the whole-tumor level, the presence of truncal gains involving 3q21.3–3q29, which GISTIC2.0 analysis¹⁸ detected as a significant peak in tumor regions with a solid pattern (Methods), and truncal *SMARCA4* mutations and/or LOH, were enriched in purely solid tumors compared to mixed solid tumors (arm/focal 3q gain, $P = 0.0011$; *SMARCA4* alterations, $P = 0.042$; Fisher's exact test; Fig. 3e,f and Extended Data Fig. 5b–i). These results suggest that purely solid tumors have genomic alterations and an evolutionary trajectory distinct from mixed solid tumors.

Growth pattern evolution from primary tumor to metastasis

To determine the relationship between growth patterns in matched primary and metastatic tumors, the phylogenies of metastatic clones were inferred in 65 participants (Fig. 4a). Metastatic tumors consisted of LNs ($n = 83$) and intrapulmonary metastasis ($n = 2$) removed at the time of primary surgery, and sites of disease relapse sampled using diagnostic biopsies or surgical resection ($n = 36$), and were subjected to centralized pathological review and subtyping (107/121 (88%), samples analyzed for growth pattern). The majority of metastatic samples displayed high-grade patterns (82/107, 77%; Fig. 4a,b). Each primary tumor region was classified as a metastasis seeding region or a metastasis non-seeding region based on phylogenetic analysis¹⁰. Seeding regions were defined as primary tumor regions harboring metastasis seeding clones, and seeding clones were defined as the most recent shared clone between the primary tumor and metastasis. In certain tumors, multiple seeding clones were identified, and in certain cases these were spread across all tumor regions. Using a numerical score, the mean grade for each seeding region was calculated and compared with the mean grade for each matched metastatic tumor region and primary tumor non-seeding regions (Fig. 4c). While no significant difference was observed using this numerical score to compare seeding and non-seeding regions in the primary tumor ($P = 0.096$, Wilcoxon signed-rank test; Fig. 4d), the metastatic regions were typically the same or showed a higher-grade pattern compared with their matched

seeding regions ($P < 0.001$, permutation test; Methods and Fig. 4e). One such example was a papillary predominant primary adenocarcinoma (CRUK0543; Fig. 4f,g) in which two of three metastatic LNs (LN_7 and LN_8), deriving from different phylogenetic branches, showed a high-grade (cribriform) pattern, while the majority (4/5) of the seeding regions showed a mid-grade (papillary) pattern, suggestive of parallel evolution of growth patterns during the metastatic cascade.

A particular case of interest involved a diagnosis of primary lepidic predominant (non-mucinous) adenocarcinoma (CRUK0296), which was found to have a pure lepidic intrapulmonary metastasis during follow-up. After primary resection, the participant developed a subsequent tumor in the contralateral lung, which was surgically resected, and a diagnosis of a pure lepidic pattern metachronous primary LUAD was made. However, TRACERx genomic profiling revealed the tumors were clonally related, indicating intrapulmonary metastasis (Extended Data Fig. 6a–d). Notably, no pure lepidic metastases were identified in a previous study of 23 intrapulmonary LUAD metastases, although both the primary and metastasis showed partial lepidic growth in 14 (61%) of the cases¹⁹. Furthermore, the CRUK0296 primary tumor demonstrated evidence of STAS (Extended Data Fig. 6c), and the presence of a confirmed metastatic lesion that is purely lepidic, and therefore without stromal invasion, supports the hypothesis that free-floating cells can seed distant tumors by aerogenous spread. There were five additional participants with a sequenced lung metastasis either at resection or during follow-up all in whom the primary tumor demonstrated STAS. Phylogenetic analysis revealed late divergence in all cases (Extended Data Fig. 6e), which was defined as the divergence of the metastatic clone after the last complete clonal sweep within the primary tumor¹⁰. Although the predominant primary tumor subtype was unrelated to the timing of metastatic divergence (Extended Data Fig. 6f), STAS positivity was significantly associated with late divergence ($P = 0.019$, Fisher's exact test; Extended Data Fig. 6g), suggesting that the ability to metastasize through airways may be a late event during LUAD evolution, or that tumors acquiring the ability to metastasize through airways early in their evolution may be rare in our surgical cohort. Overall, these findings prompted a more detailed analysis of the relationship between histological pattern, STAS and patient outcome, including the site of relapse (Extended Data Fig. 7a).

Impact of tumor morphology upon site and risk of recurrence

The morphological feature of STAS is defined as free-floating tumor cells, or tumor cell clusters, in air spaces beyond the boundary of the tumor, and is known to be associated with intrathoracic recurrence in limited (sublobar) resections in stage I LUAD^{3,20,21}, as well as poor prognosis in more advanced stage LUAD^{22,23} and non-LUAD histologies^{24,25}. In a multivariable analysis of the TRACERx 421 LUAD cohort, DFS of STAS-positive cases was shorter than that of STAS-negative cases (hazard ratio (HR) = 2.2, 95% CI 1.4–3.6; Extended Data Fig. 7b). STAS positivity was associated with the presence of high-grade patterns in each tumor ($q = 0.0075$, univariate logistic regression, ANOVA, FDR adjusted; Methods), and was associated with micropapillary pattern ($q = 0.0071$; Extended Data Fig. 7c,d), as described in other cohorts^{3,22}. Immunohistochemical nuclear beta-catenin positivity and an epithelial to mesenchymal transition (EMT) phenotype has been shown to be associated with STAS²⁶. In the TRACERx LUAD cohort, driver mutations in the Wnt pathway were enriched in STAS-positive tumors, ($q = 0.033$, Fisher's exact test, FDR adjusted; Extended Data Fig. 8a), and bulk tumor transcriptomic profiles showed higher *CTNNB1* gene expression ($P = 0.0076$, linear mixed-effect model, ANOVA; Extended Data Fig. 8b). However, we did not observe EMT pathway or Wnt– β -catenin signaling gene expression module enrichment in STAS-positive tumors (Extended Data Fig. 8c), potentially due to the difficulty of capturing phenotypic differences using bulk transcriptomic data.

The presence of preoperative ctDNA is associated with an increased risk of relapse in LUAD²⁷. In our companion paper, the presence of

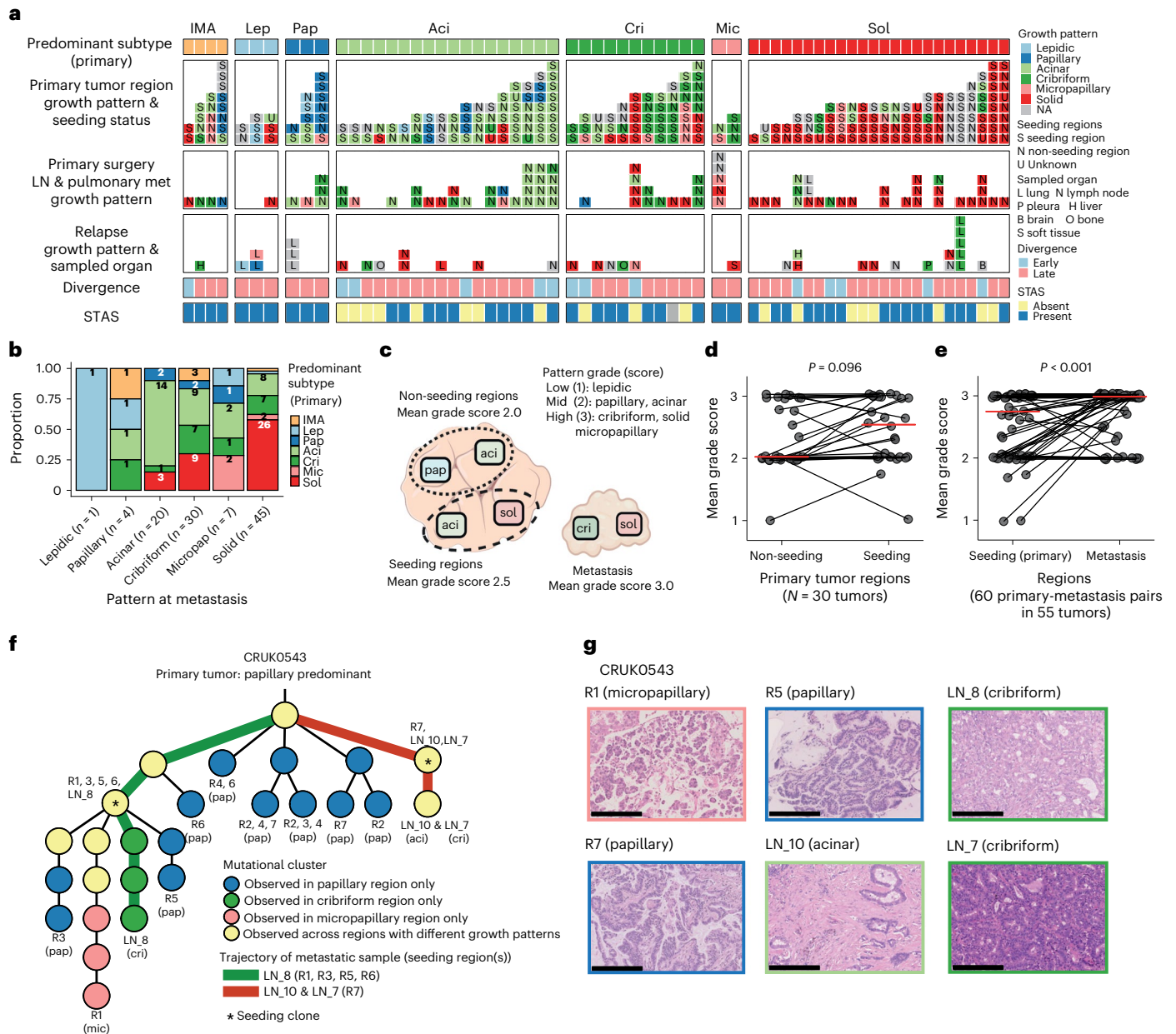


Fig. 4 | Growth pattern evolution from primary tumor to metastasis. **a**, Overview of metastasis samples in the TRACERx LUAD cohort ($n = 65$ patients). Growth pattern and the presence of seeding clones in primary tumor, growth pattern and the site of metastasis samples, timing of divergence of the metastasizing clone, and presence of the tumor STAS in the primary tumor are shown. **b**, Frequency of the observed growth pattern in metastasis samples. The x axis represents the growth pattern of metastatic samples and the color represents the predominant subtype of the primary tumor. Multiple metastasis samples from the same primary tumor are counted independently. **c**, Schematic showing the calculation of mean grade scores of non-seeding regions and seeding regions in the primary tumor, as well as metastatic samples. Grade scores of 1, 2 and 3 were given for low-grade, mid-grade and high-grade patterns, respectively, and mean scores per group were calculated for each tumor. **d**, Comparison of mean grade scores between seeding and non-seeding regions in primary tumors. Tumors harboring at least one seeding and non-seeding region with growth

pattern annotation were included in the analysis ($n = 30$ tumors). The median is indicated by the red horizontal line. A two-sided Wilcoxon signed-rank test was used. **e**, Comparison of growth pattern between metastasis and the primary tumor seeding regions (60 primary-metastasis pairs in 55 tumors). The median is indicated by the red horizontal line. To evaluate the enrichment of lower-to-higher transition of the grade score from primary to metastatic tumors, an empirical P value was calculated using a permutation test (Methods). **f**, Example of phylogenetic tree (CRUK0543) including multiple metastases to LNs resected at surgery. Each node represents a mutational cluster, and their color indicates the growth pattern observed in the primary tumor region and/or LN harboring the cluster. Asterisks represent the most recent common ancestors of primary tumor regions and metastases (seeding clones). Terminal clusters of each branch and seeding clones are annotated with the region name where the cluster is harbored. The growth pattern of the region is annotated in parentheses. **g**, Representative H&E-stained images from CRUK0543. Scale bar, 250 μm .

preoperative ctDNA is particularly associated with extra-thoracic recurrence²⁸, which may reflect the increased risk of hematogenous metastatic dissemination. In a subset of the LUAD cohort totaling 136/242 participants, preoperative ctDNA detection data were available

from two assays (53 participants with a previously reported assay⁸ and 90 participants with an assay reported in our companion paper²⁸, including 7 analyzed with both). STAS and ctDNA status were integrated to compare the biological features of these two prognostic indicators

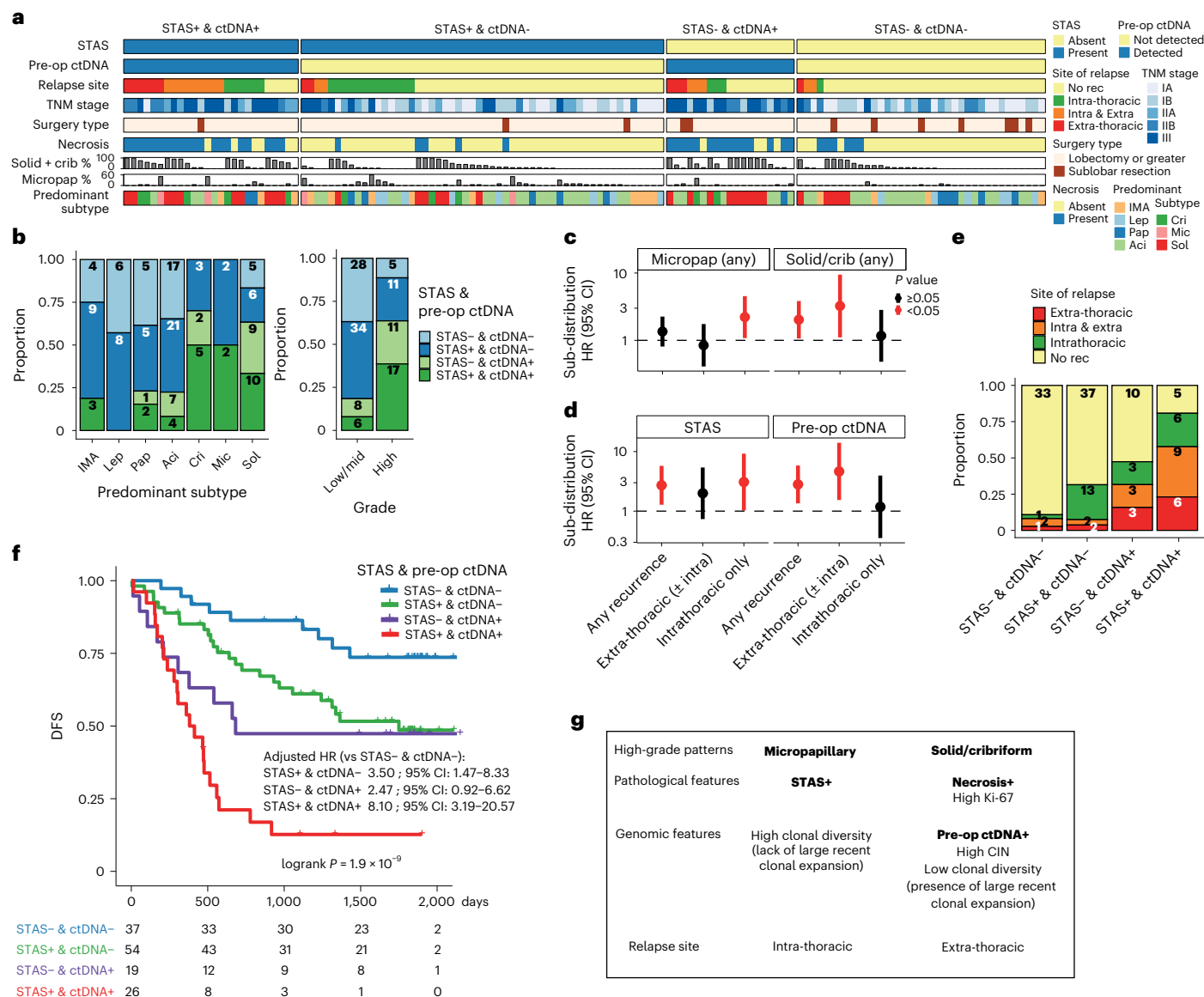


Fig. 5 | Impact of tumor morphology upon site and risk of recurrence. **a**, Overview of the TRACERx 421 LUAD cohort with STAS assessment and available preoperative ctDNA data ($n = 136$ participants), excluding the participants with synchronous primary lung cancers. Each column represents one participant. Tumors that did not relapse before death or the development of a new primary cancer were treated as no recurrence (no rec). **b**, Frequency of STAS and preoperative ctDNA positivity across predominant subtypes and grades of the predominant subtype of primary tumor. **c, d**, Relapse-site-specific (sub-distribution) HR for the presence of micropapillary patterns and the presence of solid and/or cribriform patterns (**c**; $n = 215$ participants) and the positivity of STAS and preoperative ctDNA detection (**d**) in participants with preoperative ctDNA and STAS data ($n = 131$). Participants with synchronous primary lung cancers or uncertain sites of relapse were excluded from the analyses. HRs were adjusted

for age, pathological stage, smoking pack-years, surgery type and receipt of adjuvant therapy using Fine-Gray regression model and presented with 95% CIs on a logarithmic scale. $P < 0.05$ are shown in red. No corrections were made for multiple comparisons. **e**, Frequency of the site of relapse (intrathoracic and/or extra-thoracic), stratified by the positivity of STAS and preoperative ctDNA detection. Tumors that did not relapse before death or the development of a new primary cancer are treated as no recurrence (No rec). **f**, Kaplan-Meier curves of DFS, stratified by the positivity of STAS and preoperative ctDNA detection. HRs were adjusted for age, stage, pack-years, surgery type and adjuvant therapy. The number of participants in each group for every time point is indicated below the time point. **g**, Summary of the findings related to high-grade patterns, pathological and genomic features, and relapse site. Factors with prognostic impact investigated in the study are highlighted in bold.

in relation to the risk and site of metastasis (Fig. 5a and Extended Data Fig. 7a). Participants with both STAS positivity and preoperative ctDNA detection had primary tumors enriched for predominantly high-grade patterns ($P = 7.0 \times 10^{-5}$, Fisher's exact test; Fig. 5b).

Detection of preoperative ctDNA was associated with the presence of high-grade patterns ($q = 5.4 \times 10^{-4}$, univariate logistic regression, ANOVA, FDR adjusted; Methods), in particular solid ($q = 1.0 \times 10^{-6}$) and cribriform ($q = 0.008$) patterns, and lack of lepidic ($q = 2.7 \times 10^{-5}$) and acinar patterns ($q = 0.0011$; Extended Data Fig. 7d,e). Histological

evidence of necrosis ($q = 2.2 \times 10^{-13}$), tumor size ($q = 2.8 \times 10^{-5}$) and Ki-67 fraction ($q = 9.9 \times 10^{-7}$) were associated with preoperative ctDNA detection, as previously described in TRACERx⁸, but not with STAS positivity (Extended Data Fig. 7d).

While predominantly high-grade tumors were associated with shorter DFS than predominantly low-/mid-grade tumors (HR = 1.7, 95% CI 1.1-2.6, multivariable Cox regression; Extended Data Fig. 7f), the predominance of high-grade pattern was not significantly associated with site of relapse (Extended Data Fig. 7g,h). In contrast, the presence

of a micropapillary pattern was associated with intrathoracic-only recurrence (sub-distribution HR = 2.3, 95% CI 1.1–4.7, multivariable Fine-Gray regression) and the presence of solid and/or cribriform patterns was associated with extra-thoracic recurrence (sub-distribution HR = 3.2, 95% CI 1.1–9.5; Fig. 5c), consistent with findings in stage I LUADs reported previously^{29,30}. Similarly, STAS positivity was associated with increased risk of intrathoracic-only recurrence (sub-distribution HR = 3.0, 95% CI 1.0–9.1, multivariable Fine-Gray regression), but not extra-thoracic recurrence (sub-distribution HR = 2.0, 95% CI 0.7–5.4; Fig. 5d). Notably, our cohort may be underpowered to detect the risk of extra-thoracic recurrence in STAS-positive tumors, as previously reported in a larger cohort^{22,23}. Preoperative ctDNA detection was associated with extra-thoracic recurrence (sub-distribution HR = 4.6, 95% CI 1.5–13.8, multivariable Fine-Gray regression), but not intrathoracic-only recurrence (sub-distribution HR = 1.2, 95% CI 0.3–3.9; Fig. 5d), as reported in our companion paper²⁸. Of note, STAS was detected in 17 of 21 participants (81.0%) who relapsed despite having undetectable preoperative ctDNA. This was significantly higher than STAS detection in tumors with undetectable preoperative ctDNA and no subsequent relapse (37/70, 52.8%; $P = 0.024$, Fisher's exact test; Fig. 5e and Extended Data Fig. 9a,b).

Participants with both STAS positivity and preoperative ctDNA detection had an increased risk of disease relapse compared to participants in whom neither were detected (HR = 8.1, 95% CI 3.2–20.6, multivariable Cox regression; Fig. 5f), independent of TNM staging (Extended Data Fig. 9c). Both STAS positivity and preoperative ctDNA detection were independent predictors of prognosis (STAS, HR = 3.4, 95% CI 1.8–6.4; preoperative ctDNA, HR = 2.4, 95% CI 1.3–4.2, multivariable Cox regression; Extended Data Fig. 9d). These results suggest that while STAS positivity and preoperative ctDNA detection are both associated with disease recurrence, the underlying biology of the metastatic process in tumors with each of these characteristics is distinct.

Finally, because necrosis was the histological feature most significantly associated with preoperative ctDNA detection (Extended Data Fig. 7d), we tested whether necrosis could be used as a proxy for preoperative ctDNA detection. The presence of necrosis was associated with solid and cribriform predominant tumors (solid/cribriform versus others, $P = 3.7 \times 10^{-13}$, Fisher's exact test; Extended Data Fig. 7i) and an increased risk of extra-thoracic recurrence (sub-distribution HR = 2.9, 95% CI 1.5–5.6, multivariable Fine-Gray regression), but not intrathoracic-only recurrence (sub-distribution HR = 1.6, 95% CI 0.7–3.6; Extended Data Fig. 9e,f). As a combined measure, these two histological features remained significant independent predictors of outcome in a multivariable analysis (STAS, HR = 2.4, 95% CI 1.5–3.9; necrosis, HR = 2.1, 95% CI 1.3–3.2, multivariable Cox regression; Extended Data Fig. 9g). The combination of STAS and necrosis revealed that participants with tumors positive for both had an increased risk of disease relapse (HR = 4.9, 95% CI 2.4–10.0, versus participants negative for both, multivariable Cox regression; Extended Data Fig. 9h). A similar result was observed in a larger independent external cohort of surgically resected stage IB–IIIA LUADs (Memorial Sloan Kettering Cancer Center cohort, $n = 712$, HR = 2.0, 95% CI 1.4–2.8, versus participants negative for both, multivariable Cox regression; Extended Data Fig. 10a–c).

Discussion

The exploration of the diverse growth patterns in prospectively collected multiregional and longitudinal samples, matched to the regional genomic and transcriptomic analysis performed in the TRACERx study, revealed new insights into the molecular characteristics of LUAD subtypes, which may contribute to our understanding of tumor evolution and ability to predict clinical behavior. The high-grade solid and cribriform patterns were associated with preoperative ctDNA detection and tumor necrosis, and were characterized by high chromosomal instability, cancer cell proliferation and recent subclonal expansions. These two

patterns were also associated with the development of extra-thoracic disease at recurrence, possibly reflecting an increased risk of hematogenous dissemination. Conversely, the high-grade micropapillary pattern was associated with positivity for STAS, higher subclonal diversity, suggesting an absence of a recent subclonal expansion, and the development of intrathoracic disease at recurrence possibly reflecting an increased risk of non-hematogenous dissemination (Fig. 5g). Although intercorrelations of these pathological, genomic and prognostic features are highlighted in this study, genomic and histological subtypes are not entirely interchangeable. Here, we demonstrate the clinical utility of integrated genomic and histological characterization, by combining STAS and preoperative ctDNA detection, to better predict the likelihood and site of the recurrence.

Truncal loss/LOH of chromosome 3p and 3q was enriched in predominantly low-/mid-grade tumors, suggestive of an evolutionary constraint associated with low-/mid-grade patterns. Conversely, truncal gains involving focal 3q (3q21.3–3q29) encompassing several cancer genes (*TERC*, 3q26.2; *PIK3CA*, 3q26.32) and tissue development-related and differentiation-related genes (*SOX2*, 3q26.33; *TP63*, 3q28), as well as truncal *SMARCA4* alterations, were associated with purely solid tumors. Indeed, *SMARCA4* deficiency is associated with undifferentiated thoracic carcinoma^{31–33} and arm or focal 3q gains are characteristic of lung squamous cell carcinoma rather than LUAD^{34,35}. This suggests that purely solid tumors, commonly classified histologically as LUAD based on TTF-1 immunohistochemical staining alone, may have a distinct evolutionary trajectory from mixed-pattern tumors with a solid component and harbor common genomic traits with other NSCLC histological types. Molecular profiling of undifferentiated tumors, including purely solid LUADs and non-LUAD subtypes, may improve the classification of NSCLC in relation to underlying evolutionary trajectories.

The inferred transition toward higher-grade patterns in primary tumor ancestor–descendant-like analysis and in seeding region-to-metastasis analysis may reflect the evolutionary trajectories adopted from lower-grade to higher-grade patterns. Of note, in a minority of primary tumors, we inferred subclonal evolution from higher-grade to lower-grade patterns suggesting plasticity in growth patterns, which may reflect epigenetic and/or tumor microenvironmental factors, as previously suggested³⁶. However, this may reflect parallel evolution of two regions from an ancestral 'low-grade' clone, or misassignment of evolutionary routes.

Preclinical models in other tumor types have demonstrated the impact of spatial constraints upon the pattern of tumor growth³⁷. In our cohort, LN metastatic samples are heavily represented, and this tissue type contains less structural matrix and more spatial restrictions compared with typical lung parenchyma. The shift from low-/mid-grade seeding regions in the primary tumor to high-grade metastasis may therefore be partly explained by the differing microenvironment in the primary and metastatic sites.

As previously reported, both STAS and ctDNA positivity were individually associated with poor prognosis in LUAD^{22,23,27}. STAS-positive tumors are known to be associated with locoregional recurrence after limited resection in stage I LUAD^{3,20,21}, which may reflect increased risk of non-hematogenous dissemination of tumor cells. Conversely, increased risk of extra-thoracic recurrence is observed in patients in whom preoperative ctDNA is detected²⁸, and ctDNA detection in LUAD may reflect the increased risk of hematogenous cancer cell dissemination. Indeed, the high rate of STAS positivity (81%) in participants with undetectable preoperative ctDNA who subsequently developed disease relapse, more often within the thorax, strongly suggests that STAS reflects the mechanism of metastasis seeding in tumors that do not undergo hematogenous spread.

In this cohort, it was possible to demonstrate that individuals who are positive for both STAS and preoperative ctDNA have particularly poor outcomes. As a combined measure, STAS positivity and ctDNA

Q13

Q14

detection have the potential to predict outcome at resection, differentiating the underlying mechanisms of metastatic dissemination following curative surgery. The prognostic relevance of necrosis, mitotic index and nuclear grade has been previously reported in surgically treated LUADs^{38–41}. Here, we confirmed these histological features are associated with preoperative ctDNA detection, with necrosis demonstrating the strongest association. Necrosis may therefore represent a proxy for ctDNA detection, suggesting clinical value for combined STAS and necrosis scoring in patients without available preoperative ctDNA data. We have demonstrated this largely in tumors of >2 cm, while alternative prognostic models have previously been proposed in stage IA (<2 cm) LUAD⁴².

Overall, these data reveal new aspects of the underlying biology of high-grade LUAD patterns and their increased metastatic potential, as well as detailing the differing mechanisms of metastasis adopted by tumors with specific growth patterns. Given that variable differentiation and morphology is a common feature of many cancers, the characteristics of high-grade disease described here may be relevant to other tumor types. Furthermore, these data demonstrate the relevance of measures relating to STAS, necrosis and ctDNA detection in defining patient risk stratification and predicting prognosis.

Q15

Online content

Any methods, additional references, Nature Portfolio reporting summaries, source data, extended data, supplementary information, acknowledgements, peer review information; details of author contributions and competing interests; and statements of data and code availability are available at <https://doi.org/10.1038/s41591-023-02230-w>.

References

- Nicholson, A. G. et al. The 2021 WHO classification of lung tumors: impact of advances since 2015. *J. Thorac. Oncol.* **17**, 362–387 (2022).
- Chang, J. C. et al. Comprehensive molecular and clinicopathologic analysis of 200 pulmonary invasive mucinous adenocarcinomas identifies distinct characteristics of molecular subtypes. *Clin. Cancer Res.* **27**, 4066–4076 (2021).
- Kadota, K. et al. Tumor spread through air spaces is an important pattern of invasion and impacts the frequency and location of recurrences after limited resection for small stage I lung adenocarcinomas. *J. Thorac. Oncol.* **10**, 806–814 (2015).
- Moreira, A. L. et al. A grading system for invasive pulmonary adenocarcinoma: a proposal from the international association for the study of lung cancer pathology committee. *J. Thorac. Oncol.* **15**, 1599–1610 (2020).
- Caso, R. et al. The underlying tumor genomics of predominant histologic subtypes in lung adenocarcinoma. *J. Thorac. Oncol.* **15**, 1844–1856 (2020).
- Tavernari, D. et al. Nongenetic evolution drives lung adenocarcinoma spatial heterogeneity and progression. *Cancer Discov.* **11**, 1490–1507 (2021).
- Jamal-Hanjani, M. et al. Tracking the evolution of non-small-cell lung cancer. *N. Engl. J. Med.* **376**, 2109–2121 (2017).
- Abbosh, C. et al. Phylogenetic ctDNA analysis depicts early-stage lung cancer evolution. *Nature* **545**, 446–451 (2017).
- Frankell, A. M. et al. The evolution of lung cancer and impact of subclonal selection in TRACERx. *Nature* (in press) (2023).
- Al Bakir, M. et al. The evolution of non-small lung cancer metastases in TRACERx 421. *Nature*, (in press) (2023).
- Martínez-Ruiz, C. et al. Genomic-transcriptomic evolution in lung cancer and metastasis. *Nature* (in press) (2023).
- Favero, F. et al. Sequenza: allele-specific copy number and mutation profiles from tumor sequencing data. *Ann. Oncol.* **26**, 64–70 (2015).
- Warth, A. et al. Tumour cell proliferation (Ki-67) in non-small cell lung cancer: a critical reappraisal of its prognostic role. *Br. J. Cancer* **111**, 1222–1229 (2014).
- Dong, Z.-Y. et al. Genetic and immune profiles of solid predominant lung adenocarcinoma reveal potential immunotherapeutic strategies. *J. Thorac. Oncol.* **13**, 85–96 (2018).
- Ding, Y. et al. Comparative study on the mutational profile of adenocarcinoma and squamous cell carcinoma predominant histologic subtypes in Chinese non-small cell lung cancer patients. *Thorac. Cancer* **11**, 103–112 (2020).
- Rekhtman, N., Ang, D. C., Riely, G. J., Ladanyi, M. & Moreira, A. L. KRAS mutations are associated with solid growth pattern and tumor-infiltrating leukocytes in lung adenocarcinoma. *Mod. Pathol.* **26**, 1307–1319 (2013).
- Lastwika, K. J. et al. Control of PD-L1 expression by oncogenic activation of the AKT–mTOR pathway in non-small cell lung cancer. *Cancer Res.* **76**, 227–238 (2016).
- Mermel, C. H. et al. GISTIC2.0 facilitates sensitive and confident localization of the targets of focal somatic copy number alteration in human cancers. *Genome Biol.* **12**, R41 (2011).
- Chang, J. C. et al. Comprehensive next-generation sequencing unambiguously distinguishes separate primary lung carcinomas from intrapulmonary metastases: comparison with standard histopathologic approach. *Clin. Cancer Res.* **25**, 7113–7125 (2019).
- Masai, K. et al. Prognostic impact of margin distance and tumor spread through air spaces in limited resection for primary lung cancer. *J. Thorac. Oncol.* **12**, 1788–1797 (2017).
- Eguchi, T. et al. Lobectomy is associated with better outcomes than sublobar resection in spread through air spaces (STAS)-positive T1 lung adenocarcinoma: a propensity score-matched analysis. *J. Thorac. Oncol.* **14**, 87–98 (2019).
- Warth, A. et al. Prognostic impact of intra-alveolar tumor spread in pulmonary adenocarcinoma. *Am. J. Surg. Pathol.* **39**, 793–801 (2015).
- Terada, Y. et al. Spread through air spaces is an independent predictor of recurrence in stage III (N2) lung adenocarcinoma. *Interact. Cardiovasc. Thorac. Surg.* **29**, 442–448 (2019).
- Aly, R. G. et al. Spread through air spaces (STAS) is prognostic in atypical carcinoid, large cell neuroendocrine carcinoma, and small cell carcinoma of the lung. *J. Thorac. Oncol.* **14**, 1583–1593 (2019).
- Lu, S. et al. Spread through air spaces (STAS) is an independent predictor of recurrence and lung cancer-specific death in squamous cell carcinoma. *J. Thorac. Oncol.* **12**, 223–234 (2017).
- Ikeda, T. et al. The epithelial–mesenchymal transition phenotype is associated with the frequency of tumor spread through air spaces (STAS) and a high risk of recurrence after resection of lung carcinoma. *Lung Cancer* **153**, 49–55 (2021).
- Chabon, J. J. et al. Integrating genomic features for non-invasive early lung cancer detection. *Nature* **580**, 245–251 (2020).
- Abbosh, C. et al. Phylogenetic ctDNA profiling of metastatic dissemination in lung cancer. *Nature* (in press) (2023).
- Ujii, H. et al. Solid predominant histologic subtype in resected stage I lung adenocarcinoma is an independent predictor of early, extrathoracic, multisite recurrence and of poor postrecurrence survival. *J. Clin. Oncol.* **33**, 2877–2884 (2015).
- Nitadori, J.-I. et al. Impact of micropapillary histologic subtype in selecting limited resection versus lobectomy for lung adenocarcinoma of 2cm or smaller. *J. Natl Cancer Inst.* **105**, 1212–1220 (2013).
- Rekhtman, N. et al. SMARCA4-deficient thoracic sarcomatoid tumors represent primarily smoking-related undifferentiated carcinomas rather than primary thoracic sarcomas. *J. Thorac. Oncol.* **15**, 231–247 (2020).

32. Schoenfeld, A. J. et al. The genomic landscape of SMARCA4 alterations and associations with outcomes in patients with lung cancer. *Clin. Cancer Res.* **26**, 5701–5708 (2020).
33. Concepcion, C. P. et al. *Smrca4* inactivation promotes lineage-specific transformation and early metastatic features in the lung. *Cancer Discov.* **12**, 562–585 (2022).
34. Qian, J. & Massion, P. P. Role of chromosome 3q amplification in lung cancer. *J. Thorac. Oncol.* **3**, 212–215 (2008).
35. Tonon, G. et al. High-resolution genomic profiles of human lung cancer. *Proc. Natl Acad. Sci. USA* **102**, 9625–9630 (2005).
36. Moore, D. A. et al. In situ growth in early lung adenocarcinoma may represent precursor growth or invasive clone outgrowth—a clinically relevant distinction. *Mod. Pathol.* **32**, 1095–1105 (2019).
37. Messal, H. A. et al. Tissue curvature and apicobasal mechanical tension imbalance instruct cancer morphogenesis. *Nature* **566**, 126–130 (2019).
38. Yoshizawa, A. et al. Impact of proposed IASLC/ATS/ERS classification of lung adenocarcinoma: prognostic subgroups and implications for further revision of staging based on analysis of 514 stage I cases. *Mod. Pathol.* **24**, 653–664 (2011).
39. Kadota, K. et al. A grading system combining architectural features and mitotic count predicts recurrence in stage I lung adenocarcinoma. *Mod. Pathol.* **25**, 1117–1127 (2012).
40. Mäkinen, J. M. et al. Histological features of malignancy correlate with growth patterns and patient outcome in lung adenocarcinoma. *Histopathology* **71**, 425–436 (2017).
41. von der Thüsen, J. H. et al. Prognostic significance of predominant histologic pattern and nuclear grade in resected adenocarcinoma of the lung: potential parameters for a grading system. *J. Thorac. Oncol.* **8**, 37–44 (2013).
42. Bains, S. et al. Procedure-specific risk prediction for recurrence in patients undergoing lobectomy or sublobar resection for small (≤ 2 cm) lung adenocarcinoma: An international cohort analysis. *J. Thorac. Oncol.* **14**, 72–86 (2019).

Publisher's note Springer Nature remains neutral with regard to jurisdictional claims in published maps and institutional affiliations.

Open Access This article is licensed under a Creative Commons Attribution 4.0 International License, which permits use, sharing, adaptation, distribution and reproduction in any medium or format, as long as you give appropriate credit to the original author(s) and the source, provide a link to the Creative Commons license, and indicate if changes were made. The images or other third party material in this article are included in the article's Creative Commons license, unless indicated otherwise in a credit line to the material. If material is not included in the article's Creative Commons license and your intended use is not permitted by statutory regulation or exceeds the permitted use, you will need to obtain permission directly from the copyright holder. To view a copy of this license, visit <http://creativecommons.org/licenses/by/4.0/>.

© The Author(s) 2023

Takahiro Karasaki^{1,2,3,106}, David A. Moore^{1,2,4,106}, Selvaraju Veeriah¹, Cristina Naceur-Lombardelli¹, Antonia Toncheva¹, Neil Magno¹, Sophia Ward^{1,2,5}, Maise Al Bakir^{1,2}, Thomas B. K. Watkins², Kristiana Grigoriadis^{1,2,6}, Ariana Huebner^{1,2,6}, Mark S. Hill², Alexander M. Frankell^{1,2}, Christopher Abbosh¹, Clare Puttick^{1,2,6}, Haoran Zhai^{1,2}, Francisco Gimeno-Valiente¹, Sadegh Saghafinia¹, Nnennaya Kanu¹, Michelle Dietzen^{1,2,6}, Oriol Pich², Emilia L. Lim^{1,2}, Carlos Martinez-Ruiz^{1,6}, James R. M. Black^{1,6}, Dhruva Biswas^{1,2,7}, Brittany B. Campbell², Claudia Lee², Emma Colliver², Katey S. S. Enfield², Sonya Hessey^{1,3,8}, Crispin T. Hiley^{1,2}, Simone Zaccaria^{1,8}, Kevin Litchfield^{1,9}, Nicolai J. Birkbak^{1,2,10,11,12}, Elizabeth Larose Cadieux^{13,14}, Jonas Demeulemeester^{13,15,16}, Peter Van Loo^{13,17,18}, Prasad S. Adusumilli^{19,20}, Kay See Tan²¹, Waseem Cheema¹⁹, Francisco Sanchez-Vega^{19,21}, David R. Jones¹⁹, Natasha Rekhman²², William D. Travis²², Allan Hackshaw^{19,23}, Teresa Marafioti⁴, Roberto Salgado^{24,25}, John Le Quesne^{26,27,28}, Andrew G. Nicholson^{29,30}, TRACERx Consortium*, Nicholas McGranahan^{1,6,107}, Charles Swanton^{1,2,31,107} ✉ & Mariam Jamal-Hanjani^{1,3,31,107} ✉

¹Cancer Research UK Lung Cancer Centre of Excellence, University College London Cancer Institute, London, UK. ²Cancer Evolution and Genome Instability Laboratory, The Francis Crick Institute, London, UK. ³Cancer Metastasis Lab, University College London Cancer Institute, London, UK. ⁴Department of Cellular Pathology, University College London Hospitals, London, UK. ⁵Advanced Sequencing Facility, The Francis Crick Institute, London, UK. ⁶Cancer Genome Evolution Research Group, Cancer Research UK Lung Cancer Centre of Excellence, University College London Cancer Institute, London, UK. ⁷Bill Lyons Informatics Centre, University College London Cancer Institute, London, UK. ⁸Computational Cancer Genomics Research Group, University College London Cancer Institute, London, UK. ⁹The Tumour Immunogenomics and Immunosurveillance (TIGI) Lab, University College London Cancer Institute, London, UK. ¹⁰Department of Molecular Medicine, Aarhus University Hospital, Aarhus, Denmark. ¹¹Department of Clinical Medicine, Aarhus University, Aarhus, Denmark. ¹²Bioinformatics Research Center, Aarhus University, Aarhus, Denmark. ¹³Cancer Genomics Laboratory, The Francis Crick Institute, London, UK. ¹⁴Medical Genomics, University College London Cancer Institute, London, UK. ¹⁵Integrative Cancer Genomics Laboratory, Department of Oncology, KU Leuven, Leuven, Belgium. ¹⁶VIB – KU Leuven Center for Cancer Biology, Leuven, Belgium. ¹⁷Department of Genetics, The University of Texas MD Anderson Cancer Center, Houston, TX, USA. ¹⁸Department of Genomic Medicine, The University of Texas MD Anderson Cancer Center, Houston, TX, USA. ¹⁹Thoracic Service, Department of Surgery, Memorial Sloan Kettering Cancer Center, New York, NY, USA. ²⁰Center for Cell Engineering, Memorial Sloan Kettering Cancer Center, New York, NY, USA. ²¹Department of Epidemiology and Biostatistics, Memorial Sloan Kettering Cancer Center, New York, NY, USA. ²²Department of Pathology, Memorial Sloan Kettering Cancer Center, New York, NY, USA. ²³Cancer Research UK and UCL Cancer Trials Centre, London, UK. ²⁴Department of Pathology, GZA-ZNA Hospitals, Antwerp, Belgium. ²⁵Division of Research, Peter Mac Callum Cancer Centre, Melbourne, Australia. ²⁶Cancer Research UK Beatson Institute, Glasgow, UK. ²⁷School of Cancer Sciences, University

of Glasgow, Glasgow, UK. ²⁸NHS Greater Glasgow and Clyde Pathology Department, Queen Elizabeth University Hospital, Glasgow, UK. ²⁹Department of Histopathology, Royal Brompton and Harefield Hospitals, Guy's and St Thomas' NHS Foundation Trust, London, UK. ³⁰National Heart and Lung Institute, Imperial College, London, UK. ³¹Department of Oncology, University College London Hospitals, London, UK. ¹⁰⁶These authors contributed equally: Takahiro Karasaki, David A. Moore. ¹⁰⁷These authors jointly supervised this work: Nicholas McGranahan, Charles Swanton, Mariam Jamal-Hanjani. *A list of authors and their affiliations appears at the end of the paper. ✉e-mail: nicholas.mcgranahan.10@ucl.ac.uk; charles.swanton@crick.ac.uk; m.jamal-hanjani@ucl.ac.uk

TRACERx Consortium

Charles Swanton^{1,2,31,107}, Mariam Jamal-Hanjani^{1,3,31,107}, Nicholas McGranahan^{1,6,107}, Takahiro Karasaki^{1,2,3,106}, David A. Moore^{1,2,4,106}, Selvaraju Veeriah¹, Cristina Naceur-Lombardelli¹, Antonia Toncheva¹, Sophia Ward^{1,2,5}, Maise Al Bakir^{1,2}, Thomas B. K. Watkins², Kristiana Grigoriadis^{1,2,6}, Ariana Huebner^{1,2,6}, Mark S. Hill², Alexander M. Frankell^{1,2}, Christopher Abbosh¹, Clare Puttick^{1,2,6}, Haoran Zhai^{1,2}, Francisco Gimeno-Valiente¹, Sadegh Saghafinia¹, Nnennaya Kanu¹, Michelle Dietzen^{1,2,6}, Oriol Pich², Emilia L. Lim^{1,2}, Dhruva Biswas^{1,2,7}, Brittany B. Campbell², Emma Colliver², Katey S. S. Enfield², Sonya Hessey^{1,3,8}, Crispin T. Hiley^{1,2}, Simone Zaccaria^{1,8}, Kevin Litchfield^{1,9}, Nicolai J. Birkbak^{1,2,10,11,12}, Elizabeth Larose Cadieux^{13,14}, Jonas Demeulemeester^{13,15,16}, Peter Van Looy^{13,17,18}, Allan Hackshaw²³, Teresa Marafioti⁴, Roberto Salgado^{24,25}, John Le Quesne^{26,27,28}, Andrew G. Nicholson^{29,30}, Jason F. Lester³², Amrita Bajaj³³, Apostolos Nakas³³, Azmina Sodha-Ramdeen³³, Keng Ang³³, Mohamad Tufail³³, Mohammed Fiyaz Chowdhry³³, Molly Scotland³³, Rebecca Boyles³³, Sridhar Rathinam³³, Claire Wilson³⁴, Domenic Marrone³⁴, Sean Dulloo³⁴, Dean A. Fennell^{33,34}, Gurdeep Matharu³⁵, Jacqui A. Shaw³⁵, Joan Riley³⁵, Lindsay Primrose³⁵, Ekaterini Boleti³⁶, Heather Cheyne³⁷, Mohammed Khalil³⁷, Shirley Richardson³⁷, Tracey Cruickshank³⁷, Gillian Price^{38,39}, Keith M. Kerr⁴⁰, Sarah Benafif³¹, Kayleigh Gilbert⁴¹, Babu Naidu⁴², Akshay J. Patel⁴³, Aya Osman⁴³, Christer Lacson⁴³, Gerald Langman⁴³, Helen Shackelford⁴³, Madava Djearaman⁴³, Salma Kadiri⁴³, Gary Middleton^{43,44}, Angela Leek⁴⁵, Jack Davies Hodgkinson⁴⁵, Nicola Totten⁴⁵, Angeles Montero⁴⁶, Elaine Smith⁴⁶, Eustace Fontaine⁴⁶, Felice Granato⁴⁶, Helen Doran⁴⁶, Juliette Novasio⁴⁶, Kendada Rammohan⁴⁶, Leena Joseph⁴⁶, Paul Bishop⁴⁶, Rajesh Shah⁴⁶, Stuart Moss⁴⁶, Vijay Joshi⁴⁶, Philip Crosbie^{46,47,48}, Fabio Gomes⁴⁹, Kate Brown⁴⁹, Mathew Carter⁴⁹, Anshuman Chaturvedi^{48,49}, Lynsey Priest^{48,49}, Pedro Oliveira^{48,49}, Colin R. Lindsay⁵⁰, Fiona H. Blackhall⁵⁰, Matthew G. Krebs⁵⁰, Yvonne Summers⁵⁰, Alexandra Clipson⁵¹, Jonathan Tugwood⁵¹, Alastair Kerr^{48,51}, Dominic G. Rothwell^{48,51}, Elaine Kilgour^{48,51}, Caroline Dive^{52,53}, Hugo J. W. L. Aerts^{54,55,56}, Roland F. Schwarz^{57,58}, Tom L. Kaufmann⁵⁹, Gareth A. Wilson², Rachel Rosenthal², Zoltan Szallasi^{60,61,62}, Judit Kisistok^{10,11,63}, Mateo Sokac^{10,11,63}, Miklos Diossy⁶⁴, Abigail Bunkum^{1,3,8}, Aengus Stewart⁶⁵, Alastair Magness⁶⁵, Andrew Rowan², Angeliki Karamani⁶⁶, Benny Chain⁶⁶, Carla Castignani^{13,14}, Carlos Martínez-Ruiz^{1,6}, Chris Bailey², Clare Weeden⁶⁵, Claudia Lee², Corentin Richard¹, David R. Pearce⁶⁶, Despoina Karagianni⁶⁶, Dina Levi⁶⁵, Elena Hoxha⁶⁶, Emma Nye⁶⁷, Eva Grönroos⁶⁵, Felip Gálvez-Cancino⁶⁶, Foteini Athanasopoulou^{1,2,5}, George Kassiotis^{65,68}, Georgia Stavrou⁶⁶, Gerasimos Mastrokalos⁶⁶, Helen L. Lowe⁶⁶, Ignacio Garcia Matos⁶⁶, Jacki Goldman⁶⁵, James L. Reading⁶⁶, James R. M. Black^{1,6}, Javier Herrero⁷, Jayant K. Rane^{65,66}, Jerome Nicod⁵, Jie Min Lam⁶⁶, John A. Hartley⁶⁶, Karl S. Peggs^{69,70}, Kayalvizhi Selvaraju⁶⁶, Kerstin Thol^{1,6}, Kevin W. Ng⁷¹, Kezhong Chen⁶⁶, Krijn Dijkstra⁶⁵, Krupa Thakkar¹, Leah Ensell⁶⁶, Mansi Shah⁶⁶, Marcos Vasquez Duran⁶⁶, Maria Litovchenko⁶⁶, Mariana Werner Sunderland¹, Michelle Leung⁶⁵, Mickael Escudero⁶⁵, Mihaela Angelova², Miljana Tanic^{14,72}, Monica Sivakumar¹, Olga Chervova⁶⁶, Olivia Lucas^{66,73}, Othman Al-Sawaf⁶⁶, Paulina Prymas¹, Philip Hobson⁶⁵, Piotr Pawlik⁶⁶, Richard Kevin Stone⁶⁷, Robert Bentham^{1,6}, Robert E. Hynds⁶⁶, Roberto Vendramin⁶⁵, Saioa López⁶⁶, Sam Gamble⁶⁶, Seng (Anakin) Ung⁶⁶, Sergio A. Quezada^{1,74}, Sharon Vanloo^{1,2,6}, Stefan Boeing⁶⁵, Stephan Beck¹⁴, Supreet Kaur Bola⁶⁶, Tamara Denner⁶⁵, Thanos P. Mourikis⁶⁶, Victoria Spanswick⁶⁶, Vittorio Barbé⁶⁵, Wei-Ting Lu⁶⁵, William Hill⁶⁵, Wing Kin Liu^{1,3}, Yin Wu⁶⁶, Yutaka Naito⁶⁵, Zoe Ramsden⁶⁵, Catarina Veiga⁷⁵, Gary Royle⁷⁵, Charles Fekete⁷⁶, Francesco Fraioli⁷⁷, Paul Ashford⁷⁸, Tristan Clark⁷⁹, Martin D. Forster^{1,31}, Siow Ming Lee^{1,31}, Elaine Borg⁴, Mary Falzon⁴, Dionysis Papadatos-Pastos³¹, James Wilson³¹, Tanya Ahmad³¹, Alexander James Procter⁸⁰, Asia Ahmed⁸⁰, Magali N. Taylor⁸⁰, Arjun Nair^{80,81}, David Lawrence⁸², Davide Patrini⁸², Neal Navani^{83,84}, Ricky M. Thakrar^{83,84}, Sam M. Janes⁸⁵, Emilie Martinoni Hoogenboom⁷³, Fleur Monk⁷³, James W. Holding⁷³, Junaid Choudhary⁷³, Kunal Bhakhri⁷³, Marco Scarci⁷³, Martin Hayward⁷³, Nikolaos Panagiotopoulos⁷³, Pat Gorman⁷³, Reena Khirroya⁷³, Robert C. M. Stephens⁷³, Sophia Wong⁷³, Steve Bandula⁷³, Abigail Sharp²³, Sean Smith²³, Nicole Gower²³, Harjot Kaur Dhanda²³, Kitty Chan²³, Camilla Pilotti²³, Rachel Leslie²³, Anca Grapa⁸⁶, Hanyun Zhang⁸⁶, Khalid AbdulJabbar⁸⁶, Xiaoxi Pan⁸⁶, Yinyin Yuan⁸⁶, David Chuter^{87,88,89,90}, Mairead MacKenzie⁹¹, Serena Chee⁹², Aiman Alzetani⁹², Judith Cave⁹³, Lydia Scarlett⁹², Jennifer Richards⁹², Papawadee Ingram⁹², Silvia Austin⁹², Eric Lim^{94,95}, Paulo De Sousa⁹⁶, Simon Jordan⁹⁶, Alexandra Rice⁹⁶, Hilgardt Raubenheimer⁹⁶, Harshil Bhayani⁹⁶, Lyn Ambrose⁹⁶, Anand Devaraj⁹⁶, Hema Chavan⁹⁶, Sofina Begum⁹⁶, Silviu I. Buderu⁹⁶, Daniel Kaniu⁹⁶, Mpho Malima⁹⁶, Sarah Booth⁹⁶, Nadia Fernandes⁹⁶, Pratibha Shah⁹⁶, Chiara Proli⁹⁶, Madeleine Hewish^{97,98}, Sarah Danson⁹⁹, Michael J. Shackcloth¹⁰⁰, Lily Robinson¹⁰¹, Peter Russell¹⁰¹, Kevin G. Blyth^{27,102,103}, Craig Dick¹⁰⁴, Alan Kirk¹⁰⁵, Mo Asif¹⁰⁵, Rocco Bilancia¹⁰⁵, Nikos Kostoulas¹⁰⁵ & Mathew Thomas¹⁰⁵

³²Singleton Hospital, Swansea Bay University Health Board, Swansea, UK. ³³University Hospitals of Leicester NHS Trust, Leicester, UK. ³⁴University of Leicester, Leicester, UK. ³⁵Cancer Research Centre, University of Leicester, Leicester, UK. ³⁶Royal Free Hospital, Royal Free London NHS Foundation Trust, London, UK. ³⁷Aberdeen Royal Infirmary NHS Grampian, Aberdeen, UK. ³⁸Department of Medical Oncology, Aberdeen Royal Infirmary NHS Grampian, Aberdeen, UK. ³⁹University of Aberdeen, Aberdeen, UK. ⁴⁰Department of Pathology, Aberdeen University School of Medicine, Aberdeen, UK. ⁴¹The Whittington Hospital NHS Trust, London, UK. ⁴²Birmingham Acute Care Research Group, Institute of Inflammation and Ageing, University of Birmingham, Birmingham, UK. ⁴³University Hospital Birmingham NHS Foundation Trust, Birmingham, UK. ⁴⁴Institute of Immunology and Immunotherapy, University of Birmingham, Birmingham, UK. ⁴⁵Manchester Cancer Research Centre Biobank, Manchester, UK. ⁴⁶Wythenshawe Hospital, Manchester University NHS Foundation Trust, Manchester, UK. ⁴⁷Division of Infection, Immunity and Respiratory Medicine, University of Manchester, Manchester, UK. ⁴⁸Cancer Research UK Lung Cancer Centre of Excellence, University of Manchester, Manchester, UK. ⁴⁹The Christie NHS Foundation Trust, Manchester, UK. ⁵⁰Division of Cancer Sciences, The University of Manchester and The Christie NHS Foundation Trust, Manchester, UK. ⁵¹Cancer Research UK Manchester

Institute, University of Manchester, Manchester, UK. ⁵²CRUK Manchester Institute Cancer Biomarker Centre, University of Manchester, Macclesfield, UK. ⁵³CRUK Lung Cancer Centre of Excellence, University of Manchester, Macclesfield, UK. ⁵⁴Artificial Intelligence in Medicine (AIM) Program, Mass General Brigham, Harvard Medical School, Boston, MA, USA. ⁵⁵Department of Radiation Oncology, Brigham and Women's Hospital, Dana-Farber Cancer Institute, Harvard Medical School, Boston, MA, USA. ⁵⁶Radiology and Nuclear Medicine, CARIM & GROW, Maastricht University, Maastricht, the Netherlands. ⁵⁷Institute for Computational Cancer Biology, Center for Integrated Oncology (CIO), Cancer Research Center Cologne Essen (CCCE), Faculty of Medicine and University Hospital Cologne, University of Cologne, Cologne, Germany. ⁵⁸Berlin Institute for the Foundations of Learning and Data (BIFOLD), Berlin, Germany. ⁵⁹Berlin Institute for Medical Systems Biology, Max Delbrück Center for Molecular Medicine in the Helmholtz Association (MDC), Berlin, Germany. ⁶⁰Danish Cancer Society Research Center, Copenhagen, Denmark. ⁶¹Computational Health Informatics Program, Boston Children's Hospital, Boston, MA, USA. ⁶²Department of Bioinformatics, Semmelweis University, Budapest, Hungary. ⁶³Bioinformatics Research Centre, Aarhus University, Aarhus, Denmark. ⁶⁴Department of Physics of Complex Systems, ELTE Eötvös Loránd University, Budapest, Hungary. ⁶⁵The Francis Crick Institute, London, UK. ⁶⁶University College London Cancer Institute, London, UK. ⁶⁷Experimental Histopathology, The Francis Crick Institute, London, UK. ⁶⁸Department of Infectious Disease, St Mary's Hospital, Imperial College London, London, UK. ⁶⁹Department of Haematology, University College London Hospitals, London, UK. ⁷⁰Cancer Immunology Unit, Research Department of Haematology, University College London Cancer Institute, London, UK. ⁷¹Retroviral Immunology Group, The Francis Crick Institute, London, UK. ⁷²Experimental Oncology, Institute for Oncology and Radiology of Serbia, Belgrade, Serbia. ⁷³University College London Hospitals, London, UK. ⁷⁴Immune Regulation and Tumour Immunotherapy Group, Cancer Immunology Unit, Research Department of Haematology, University College London Cancer Institute, London, UK. ⁷⁵Department of Medical Physics and Bioengineering, University College London Cancer Institute, London, UK. ⁷⁶Department of Medical Physics and Biomedical Engineering, University College London, London, UK. ⁷⁷Institute of Nuclear Medicine, Division of Medicine, University College London, London, UK. ⁷⁸Institute of Structural and Molecular Biology, University College London, London, UK. ⁷⁹University College London, London, UK. ⁸⁰Department of Radiology, University College London Hospitals, London, UK. ⁸¹UCL Respiratory, Department of Medicine, University College London, London, UK. ⁸²Department of Thoracic Surgery, University College London Hospital NHS Trust, London, UK. ⁸³Lungs for Living Research Centre, UCL Respiratory, University College London, London, UK. ⁸⁴Department of Thoracic Medicine, University College London Hospitals, London, UK. ⁸⁵Lungs for Living Research Centre, UCL Respiratory, Department of Medicine, University College London, London, UK. ⁸⁶The Institute of Cancer Research, London, UK. ⁸⁷Independent Cancer Patient Advocate, Bognor Regis, UK. ⁸⁸Digestive Cancers Europe, Brussels, Belgium. ⁸⁹NHS Leadership Academy, Leeds, UK. ⁹⁰NIHR Academy, London, UK. ⁹¹Independent Cancer Patients Voice, London, UK. ⁹²University Hospital Southampton NHS Foundation Trust, Southampton, UK. ⁹³Department of Oncology, University Hospital Southampton NHS Foundation Trust, Southampton, UK. ⁹⁴Academic Division of Thoracic Surgery, Imperial College London, London, UK. ⁹⁵The Royal Brompton Hospital, Royal Brompton and Harefield NHS Foundation Trust, London, UK. ⁹⁶Royal Brompton and Harefield NHS Foundation Trust, London, UK. ⁹⁷Royal Surrey Hospital, Royal Surrey Hospitals NHS Foundation Trust, Guildford, UK. ⁹⁸University of Surrey, Guilford, UK. ⁹⁹Sheffield Teaching Hospitals NHS Foundation Trust, Sheffield, UK. ¹⁰⁰Liverpool Heart and Chest Hospital, Liverpool, UK. ¹⁰¹Princess Alexandra Hospital, The Princess Alexandra Hospital NHS Trust, Harlow, UK. ¹⁰²Beatson Institute for Cancer Research, University of Glasgow, Glasgow, UK. ¹⁰³Queen Elizabeth University Hospital, Glasgow, UK. ¹⁰⁴NHS Greater Glasgow and Clyde, Glasgow, UK. ¹⁰⁵Golden Jubilee National Hospital, Clydebank, UK.

Methods

The TRACERx 421 cohort, sample collection and DNA/RNA sequencing

All participants were enrolled into the TRACERx study (NCT01888601, approved by an independent research ethics committee, 13/LO/1546), and underwent multiregional sampling of tumors. Written informed consent was obtained from all the participants. The first 421 participants, which constitutes the first half of the originally scheduled full cohort of the clinical trial, are included in the TRACERx 421 cohort. Inclusion/exclusion criteria of the clinical study, clinical data acquisition, DNA and RNA extraction, WES and RNA-seq, bioinformatic processing of WES and RNA-seq data, plasma sample acquisition and preoperative ctDNA analysis are described in our companion papers^{9–11,28}.

Histopathological assessment

Central histopathological review. The diagnostic slides from all LUAD cases in the cohort were requested from the local pathology departments, scanned using a Hamamatsu NanoZoomer S210 slide scanner at $\times 40$ scanning magnification and retained within a central digital histology archive. In a small number of cases, full diagnostic slides were not available and therefore pathology review was conducted using a combination of a single representative diagnostic slide and regional TRACERx tissue samples. Full diagnostic slides were used for central pathology review to confirm tumor subtype and to generate adenocarcinoma growth pattern fractions following review by central study pathologists. Tumors were categorized into six growth patterns—the five patterns currently defined in the World Health Organization (WHO) classification⁴³, with the addition of a cribriform pattern, which has elsewhere been included as part of the acinar growth pattern subtype. As per standard clinical diagnostic practice and current guidance, we labeled each tumor using the predominant histological subtype according to the proportions of each growth pattern. IMA (including mixed invasive mucinous and non-mucinous adenocarcinoma) was labeled as a separate entity, in line with the WHO classification, although pattern proportions of the six growth patterns were still ascribed. For 28/242 patients whose full diagnostic slides were not available, pattern proportion was based upon local histopathology reporting, provided this matched broadly with the appearances of any available material at central review. Any discrepancy in tumor type between the clinical pathology report and central review was subjected to additional expert review for a final definitive diagnosis. The presence of STAS was defined as previously described^{3,25}.

Nuclear grade and mitotic index. The nuclear grade was determined based upon nuclear size in the highest-grade area of the tumor, as previously described⁴¹. The mitotic index was determined from diagnostic material from the area of the tumor with the highest mitotic activity. The count was performed over a 2.4-mm² area of tumor on scanned slides, equal to the area of ten high-power microscopic fields used in previous LUAD grading studies³⁹.

Regional growth pattern annotation. Where regional fresh tissue samples were sufficient, samples were split between fresh frozen tissue for DNA and RNA extraction, and formalin-fixed paraffin-embedded tissue to allow histological assessment of the sequenced regions. This regional histology was used to generate regional growth pattern data in LUAD and regional stromal TIL scores for the entire cohort.

Definition of tumor growth pattern homogeneity. A tumor was defined as morphologically homogeneous when the tumor met both of the following criteria: (1) predominant subtype was dominating 90% or more of the tumor area in diagnostic slides and (2) predominant subtype was dominating 90% or more of the annotated regional patterns.

Growth pattern annotation in the metastatic sample. In metastatic disease, where possible, the metastatic tumor was sampled for sequencing analysis. If sufficient tissue was available for histological assessment, growth pattern was also characterized in LUAD samples. Biopsy samples that were too limited for growth pattern annotation or were too dissociated, such as some aspirated samples, were excluded from the analysis.

PD-L1 and Ki-67 immunohistochemical staining. PD-L1 (22C3 clone) and Ki-67 (MIB-1 clone) immunohistochemistry were performed on a single representative diagnostic formalin-fixed paraffin-embedded tissue block from the resection specimen using a Link48 Autostainer (Agilent) for PD-L1 and a BOND-III Autostainer (Leica Biosystems) for Ki-67, according to the manufacturer's instructions. Fractions of positively stained tumor cells (cancer cells) were scored manually by a pathologist in line with clinical guidelines.

Pathology tumor-infiltrating lymphocyte estimates. TILs were estimated from H&E-stained slides using established international guidelines, developed by the International Immuno-Oncology Biomarker Working Group, as described in the previous reports^{44–46}. In brief, the relative proportion of stromal area to tumor area was determined from the pathology slide of a given tumor region. TILs were reported for the stromal compartment (equals the percentage of stromal TILs). The denominator used to determine the percentage of stromal TILs was the area of stromal tissue. Therefore, the percentage of stromal TILs equaled the area occupied by mononuclear inflammatory cells over the total intra-tumoral stromal area rather than the fraction of total stromal nuclei that represent mononuclear inflammatory cell nuclei. This method has been demonstrated to be reproducible among trained pathologists⁴⁷. The International Immuno-Oncology Biomarker Working Group developed a freely available training tool to train pathologists for optimal TIL assessment on H&E slides (<http://www.tilsincancer.org/>).

TRACERx analytical pipeline and orthogonal method for SCNA profiling and clonality inference

Somatic copy number alteration profiling. In the TRACERx WES pipeline, copy number segmentation data were produced using ASCAT⁴⁸ and then a multi-sample SCNA estimation approach⁴⁹ was applied in which single-nucleotide polymorphisms are phased onto paternal and maternal alleles using samples with allelic imbalance and detectable B-allele-frequency separation. This approach allowed copy number aberrations present in one region to be tested for in other regions and enabled us to more accurately profile copy number states in low-purity tumor regions. To determine genome-wide copy number gain and loss events, copy number data for each sample were divided by the sample mean ploidy, and \log_2 transformed. Amplification, gain and loss thresholds were defined as $\log_2(4/2)$, $\log_2(2.5/2)$ and $\log_2(1.5/2)$, respectively. LOH was defined as a floating-point copy number of the minor allele of <0.5 . As discussed⁷, our pipeline may be under-calling homozygous deletions, due to the nature of the relatively low resolution of the WES data (restricted to exonic regions) making it difficult to call very focal events. Therefore, we excluded homozygous deletions from the analysis.

Clonality inference. In the TRACERx WES pipeline, mutations were classified as truncal or subclonal using a modified version of PyClone(v0.13.1)⁵⁰. Several additional steps were then carried out during phylogenetic tree building to avoid over-calling subclonality and inappropriately increasing the reported degree of ITH⁷⁹. For copy number amplification, we called ubiquitous amplifications truncal (for example, amplification observed in all regions for each tumor). Truncal/subclonal chromosomal arm gain and loss were defined on a per-tumor basis, by requiring at least one region to show at least 98%

gain or loss of the arm. Truncal arm gain or loss was then called if the same chromosomal arm showed at least 75% gain or loss across all remaining regions.

Orthogonal methods. As an orthogonal method for SCNA profiling, we used the default output of Sequenza¹² for each sample. As a default output, Sequenza returns integer copy numbers for major and minor alleles. LOH was defined as integer copy number = 0 for the minor allele and integer copy number > 0 for the major allele. As an alternative method to call clonality for mutations, we called ubiquitous mutations truncal, and non-ubiquitous mutations subclonal.

Enumeration of chromosomal complexity, clonal architecture and intra-tumoral heterogeneity

Weighted genome instability index. The wGII score was calculated as the proportion of the genome with copy number aberrations relative to the median ploidy, weighted on a per-chromosome basis⁵¹.

Fraction of genome subject to loss of heterozygosity. The FLOH score was defined as the proportion of the genome subject to loss of heterozygosity.

Percentage subclonal SCNA. The percentage of the genome subject to subclonal SCNA (SCNA minus ITH) events was divided by the percentage of the genome involved in any SCNA event in each tumor⁷⁹.

Subclonal TMB (clonal in ≥ 1 region; ‘illusion of clonality’-type subclonal mutation burden). Mutational clusters used for phylogenetic tree building were determined to be subclonal or clonal within every region by testing whether CCF (fraction of cancer cells harboring the cluster of mutations) was significantly lower than one. TMB of regionally clonal mutations in ≥ 1 region but not in all regions (that is, subclonal at tumor level), previously described as ‘illusion of clonality’ mutations because they may appear as clonal when only one region is sampled per tumor⁷⁹, was calculated for each tumor.

Subclonal diversity within the tumor region. First, cancer cell clone proportions, namely what percentage of the cells in that region come from each clone, were calculated using the CCF of each mutational cluster that was used for phylogenetic tree construction. Then, the Simpson Diversity Index of the clone proportions was calculated to give the subclonal diversity of each region. Minimum subclonal diversity within the tumor region was used to represent the subclonal diversity per tumor⁹.

Recent subclonal expansion score. A recent subclonal expansion score per tumor, reflecting the size of the largest recent subclonal expansion within each tumor region, was calculated as follows⁹. First, for each tumor phylogenetic tree (default tree output per tumor), the terminal nodes on the tree (that is, leaf nodes) were identified. Then, for each tumor region, the maximum CCF of any of these leaf nodes was identified. Lastly, as a tumor-level metric, the subclonal expansion score was calculated by taking the maximum across the regional scores, therefore describing the maximal size of the most recent subclone expansion in each tumor.

Genomic determinants of predominant subtype

Truncal genomic alterations associated with predominantly high-grade or low-/mid-grade tumors. To investigate the truncal genomic alterations associated with predominantly high-grade pattern tumors, we first compiled recurrent truncal events observed in more than 5% of the tumors and in at least ten tumors in either predominantly high-grade or low-/mid-grade tumors in the TRACERx 421 LUAD cohort. The compiled list was composed of 8 truncal driver alterations (6 mutations, 2 amplifications) and 31 truncal chromosomal

arm SCNAs (8 gains and 23 loss/LOHs). Logistic regression analysis was performed to construct a model to distinguish between predominantly high-grade and low-/mid-grade tumors. Specifically, we constructed an initial model with the presence/absence of these 39 truncal events as explanatory variables. Stepwise model simplification was performed using the stepAIC function (MASS (v7.3-55) R package). The final model was composed of 11 truncal genomic alterations, of which 7 were determined to be significantly independent variables. Type II ANOVA was performed on the final model using ANOVA function in the car (v3.1-0) R package. We observed consistent results when only truncal alterations observed in at least 10% of the cohort were included in the analysis, when an orthogonal tool (Sequenza¹²) for SCNA profiling was applied, or when wGII was added to the final model as a covariate to control for general genomic instability.

Differential copy number analysis of driver genes and chromosomal arms between predominantly high-grade and low-/mid-grade tumors. To capture SCNAs with a frequency in the cohort of lower than 5%, we also compared the ploidy-adjusted copy number of driver genes and chromosomal arms between predominantly high-grade and low-/mid-grade tumors. To account for multiregional input from a single tumor, a linear mixed-effect model was applied (response variable = ploidy-adjusted copy number of each SCNA, fixed effect = predominant subtype (high grade versus low/mid grade), random effect = tumor ID), using the lme function in nlme (v3.1-155) R package. An ANOVA was performed between the full model and a null model considering only the random effect, using the ANOVA function implemented in R (v3.6.1). ANOVA *P* values were adjusted for multiple comparisons using the BH method⁵². We observed consistent results when Sequenza¹² was applied for SCNA profiling, or when wGII was added to the linear mixed-effect model as a covariate.

Mutual exclusivity and co-occurrence of truncal genomic alterations associated with predominantly high-grade or low-/mid-grade tumors. To determine significantly mutually exclusive and co-occurring relationships between recurrent truncal genomic alterations observed in more than 5% of the tumors in the TRACERx 421 LUAD cohort, the Rediscover (v0.3.0) R package, which applies statistical analysis based on the Poisson binomial distribution to take into account the alteration rate of genes and samples, was implemented⁵³. The truncal events observed in at least ten tumors in either predominantly high-grade or low-/mid-grade tumors were included in the analysis. A getMutex function was applied, with a binary matrix of the presence/absence of truncal driver gene mutations and a binary matrix of truncal SCNA alterations (driver gene amplifications, chromosome arm gains and arm loss/LOH) provided as input data, for the predominantly low-/mid-grade tumors and predominantly high-grade tumors separately. A getMutexAB function was also run, with binary matrices of the presence/absence of truncal driver gene mutations and truncal SCNA alterations provided as input data. The outputs from getMutex and getMutexAB functions were combined, and the probabilities of mutual exclusivity and co-occurrence were adjusted for multiple comparisons using the BH method. To explore the mutually exclusive or co-occurring truncal events specific to either predominantly high-grade or predominantly low-/mid-grade tumors, the pairs of truncal events with unadjusted *P* values < 0.05 in both predominantly high-grade and low-/mid-grade tumors were filtered out. Analyses were conducted using R 4.0.0 (R Foundation for Statistical Computing). The same analyses were conducted including only truncal alterations observed in at least 10% of the cohort or using Sequenza¹² as an orthogonal tool for SCNA profiling.

GISTIC2.0 peak identification for tumor regions with solid pattern

GISTIC2.0 (ref.¹⁸) uses as input a copy number profile across the genome from one sample for each tumor. To investigate genomic regions of

recurrent gains and amplifications associated with a solid pattern, the copy number profiles from all solid-pattern regions from the same tumor were uniformly segmented by taking minimum consistent segmentations and the single sample copy number profile for each tumor was constructed by selecting the minimum ploidy-corrected total copy number per segment across the genome. By taking the minimum ploidy-corrected total copy number per segment, a significant peak ($q < 0.05$) in chromosome 3q (hg19 chr3: 131,091,386–191,871,390, 3q21.3–3q29) was inferred as a truncal focal amp/gain peak associated with the presence of the solid-pattern regions. To investigate the presence of the gain involving the focal 3q segment in each tumor region, mean ploidy-adjusted copy number of the focal 3q segment was calculated and \log_2 transformed. When all tumor regions harbored a mean ploidy-adjusted copy number $> \log_2(2.5/2)$, the tumor was classified as having a truncal gain of the focal 3q segment (including chromosome 3q arm gain), and the tumor was classified as having subclonal gain when not all but at least one region harbored a gain of the segment.

Gene expression data analysis and gene-set enrichment analyses

RSEM (v1.3.3) R package⁵⁴ was used with default parameters to quantify gene expression based on the BAM files aligned to the transcriptome. RSEM raw read counts were first normalized using the median of ratios method implemented in DESeq2 (v1.24.0) R package⁵⁵. Genes with more than at least five read counts below five in at least 20% of the TRACERx 421 cohort (a total of 20,136 genes) were kept after filtering. Variant stabilizing transformation was performed on the normalized reads implemented in DESeq2. The median value of the variant stabilizing transformed (VST) count of each gene was calculated per tumor, and gene-set enrichment analyses were performed using the fgseaLabel function (fgsea (v1.12.0) R package⁵⁶) to compare differentially expressed gene sets between predominantly high-grade-tumors and predominantly low-/mid-grade tumors, and between STAS-present and STAS-absent tumors using the Molecular Signatures Database hallmark gene sets⁵⁷. The biological process category of each gene set was based on the paper by Liberzon et al⁵⁷. Multiple comparisons were adjusted by the BH method and gene sets with $q < 0.25$ were determined to be significantly enriched as described elsewhere⁵⁸. Gene-set variation analysis (GSVA) score of Hallmark G2M checkpoint genes⁵⁷ was calculated for each sample using GSVA (v1.34.0) R package⁵⁹ using VST count data as input. A linear mixed-effect model was applied for the comparison of *CTNNB1* gene expression and GSVA score of G2M checkpoint genes between STAS-present and STAS-absent tumors to account for multiple regional pairs from a single tumor (response variable = VST normalized count data or GSVA score per sample, fixed effect = STAS status, random effect = tumor ID), using the lme function in nlme (v3.1-155) R package.

Enrichment analysis of G2M checkpoint gene SCNA

Mean ploidy-adjusted copy number of each gene was calculated per tumor region and was compared between predominantly high-grade tumors and predominantly low-/mid-grade tumors using a linear mixed-effect model by setting the ploidy-adjusted copy number of each gene as a response variable, predominance of growth pattern (high versus low/mid) as a fixed-effect variable, and tumor ID as a random effect using the lme function in nlme (v3.1-155) R package. ANOVA *P* values were adjusted for multiple comparisons by the BH method and the genes with $q < 0.05$ were determined to have significantly different ploidy-adjusted copy numbers between predominantly high-grade and low-/mid-grade tumors. Among the 23,657 genes tested, 2,169 were significantly gained and 2,862 were lost in predominantly high-grade tumors. Overrepresentation of G2M checkpoint genes⁵⁷ with higher copy number in predominantly high-grade tumors compared with low-/mid-grade tumors was tested by Chi-square test using the chisq.test function implemented in R (version 3.6.1).

Identification of factors independently associated with tumor cell PD-L1 expression

To investigate whether the proportion of solid pattern per tumor (solid-pattern percentage) is independently associated with tumor cell (cancer cell) PD-L1 protein expression (0% versus $\geq 1\%$), we performed multivariable logistic regression analysis (response variable = PD-L1 protein expression) to account for potential confounders. The number of TILs (pathology TIL scores), the truncal and subclonal neoantigen burden and the solid-pattern percentage were included in the model as explanatory variables.

Neoantigen prediction

Participant-specific HLA haplotype predictions were obtained using HLA-HD⁶⁰ (v1.2.1). NetMCHpan-4.1 (ref.⁶¹) was run on 9–11 neopeptides derived from nonsynonymous mutations across the TRACERx 421 cohort and taking into account participant-specific human leukocyte antigens (HLAs). A cutoff of 0.5 in the eluted ligand rank was applied to define whether a peptide was bound to a specific HLA type. An observed nonsynonymous mutation is deemed a neoantigen binding to a specific HLA if at least one of its neopeptides is considered a binder.

Genomic distance

The genomic distance using mutations was calculated as previously described⁴⁴. In brief, all detected mutations (single-nucleotide variants and indels) present in any region of a tumor were turned into a binary matrix (1, mutation present; 0, mutation absent), in which the rows were the mutations and the columns were tumor regions. The pairwise Euclidean distance between any two tumor regions within each tumor was calculated. The genomic distance using LOH was calculated similarly; in brief, the presence of cytoband-level LOH was first assigned when the copy number status of the largest genomic segment overlapping each cytoband was LOH. Then, all copy number states per cytoband in any region from a tumor were turned into a binary matrix (1, LOH present; 0, LOH absent), in which the rows were genomic segments (cytoband) and the columns were tumor regions, and the pairwise Euclidean distance between any two tumor regions was calculated. Mixed-effects models are regression analyses for repeated data measures (for example, where one participant provides multiple outcomes), and a linear mixed-effect model was applied for the comparison of genomic distances between regional pairs with same versus different growth patterns to account for multiple regional pairs from a single tumor (response variable = genomic distance, fixed effect = growth pattern (different versus same), random effect = tumor ID), using the lme function in nlme (v3.1-155) R package.

Sequential evolution from lower-grade pattern to higher-grade pattern

Application of grade pattern scoring. To compare the regional growth patterns between specific groups of regions (for example, seeding versus non-seeding regions in the primary tumor, or seeding regions versus metastasis samples), growth patterns were transformed into integer scores as follows: lepidic, 1 (low-grade pattern); papillary and acinar, 2 (mid-grade pattern); and cribriform, micropapillary and solid, 3 (high-grade pattern). The mean of regional pattern grade scores was then calculated for each regional group within each tumor.

Ancestor–descendant-like relationship inference. Within the primary tumors, regional pairs in which ancestor–descendant-like relationships were observed were investigated. In particular, we aimed to identify instances where one region in a regional pair contained a common ancestral-like clone with the other containing a descendant-like clone of the common ancestral clone. Assignments of ancestor-like regions and descendant-like regions were made as follows:

1. First, primary tumor regions with purity < 0.15 were removed to mitigate against non-robust LOH calling in low-purity regions;

2. Next, an LOH tree was built for all regional pairs by counting shared (=trunk) LOH and private (=branch) LOH events per cytoband;
3. Based on the hypothesis that the majority of LUAD tumors harbor one or more truncal arm-level LOH events, and that regional pairs that apparently harbored no shared arm-level LOH may in fact result from technical errors (for example, inappropriate ploidy/purity solutions), only LOH trees with at least one shared arm-level LOH (defined as $\geq 75\%$ of the chromosome arm being lost¹⁰) were retained for further analysis;
4. For the remaining regional pairs and LOH trees,
 - a. An ancestor-like region, namely a region that harbored a clone similar to a recent common ancestral clone, was defined as a region with a proportion of the number of private LOH less than $x\%$ (that is, private LOH / total LOH per region $< x\%$). $x = 1, 2$ and 5 were explored and $x = 2$ was used in the main text and figures.
 - b. A descendant-like region was defined as a region with a proportion of the number of private LOH greater than $y\%$ (that is, private LOH / total LOH per region $> y\%$) and more than one arm-level private LOH. $y = 7.5, 10$ and 15 were explored and $y = 10$ was used in the main text and figure.

To test if the ancestor–descendant-like relations inferred by the LOH profile conflicted with mutational profiles, dominant mutations with CCF $\geq 95\%$ (namely, mutations shared among $\geq 95\%$ cancer cells within each region) were compared between paired descendant-like regions and ancestor-like regions.

Ancestor–descendant-like regional pairs were also inferred using both LOH and mutational profiles together, applying the same method for dominant mutations (mean CCF of mutational cluster $\geq 95\%$, calculated upon phylogenetic tree construction). A mutation tree (only including mutations with mean cluster CCF $\geq 95\%$) was built for all regional pairs by counting shared mutations (trunk) and private mutations (branch). The ancestor-like region was defined as having a proportion of private mutational branch length less than 2% (that is, private mutation / total mutation per region $< 2\%$), and the descendant-like region was defined as having a proportion of private mutational branch length greater than 10% . In the combined method, considering both LOH and mutational profiles, the regional pairs identified as having ancestor–descendant-like relations by both methods were inferred as ancestor–descendant-like regional pairs. Additionally, ancestor–descendant-like regional pairs were inferred using LOH profiles called by an orthogonal tool (Sequenza¹²).

Permutation test. To test the enrichment of higher-grade patterns in the descendant-like regions and the enrichment of higher mutational burden (CCF $\geq 95\%$) in the descendant-like regions (namely, lower-to-higher (upward) transition in grade and mutation burden), permutation tests were applied to obtain empirical P values using the Monte-Carlo procedure⁶². Firstly, the number of ancestor–descendant-like regional pairs with the upward transition was counted (observed frequency). Next, for each permutation, regional growth patterns and regional mutational burdens were randomized within each tumor and the frequency of upward transition was compared against the observed frequency. Finally, the empirical P value was calculated by equation (1):

$$P = (r + 1) / (n + 1) \quad (1)$$

where r is the number of permutations that produced the same or a higher frequency of the upward transition compared with the observed frequency and n is the number of permutations.

Similarly, to test the enrichment of higher mean grade pattern scores in metastasis, a permutation test was applied to obtain empirical P values using the Monte-Carlo procedure, to account for several

tumors having multiple metastatic samples at different time points and organs. Firstly, the number of seeding region and metastasis pairs with the metastasis having higher mean grade pattern scores (namely, upward transition) was counted (observed frequency). Next, for each permutation, mean grade pattern scores were randomized within each seeding region and metastasis pair. Then, the frequency of the upward transition was compared against the observed frequency. Finally, the empirical P value was calculated by equation (1).

Histological factors associated with tumor cell spread through air spaces and preoperative circulating tumor DNA positivity

To elucidate the biological difference between STAS positivity and preoperative ctDNA positivity, a univariable logistic regression model was applied. For the response variable, either STAS positivity or preoperative ctDNA positivity was used. For the explanatory variable, each of the following histological variables was included in the model: the presence of each growth pattern, mitotic index, nuclear grade, Ki-67 fraction of tumor cells, type of tumor (IMA or not), presence of necrosis, presence of lymphovascular invasion, presence of visceral pleural invasion and pathological tumor size. P values of ANOVA in each univariable model were adjusted for multiple comparisons by the BH method.

Survival analysis (TRACERx cohort)

DFS was defined as the period from the date of registration to the time of radiological confirmation of the recurrence of the primary tumor registered for the TRACERx or the time of death by any cause. During the follow-up, three participants with LUAD (CRUK0512, CRUK0428 and CRUK0511) developed new primary cancer and subsequent recurrence from either the first primary lung cancer or the new primary cancer diagnosed during the follow-up. These cases were censored at the time of the diagnosis of new primary cancer for DFS analysis, due to the uncertainty of the origin of the third tumor. As for the participants who harbored synchronous multiple primary lung cancers, when associating genomic/pathological data from the tumors with participant-level clinical information, we used only data from the tumor of the highest pathological TMN stage. HRs and P values were calculated using the coxph function (survival (v3.4.0) R package), through multivariable Cox regression analyses, adjusted for age, pathological stage (1, 2 and 3), smoking pack-years, surgery type (sublobar resection versus lobectomy or greater) and a receipt of adjuvant therapy. Kaplan–Meier plots were generated using the ggsurvplot function (survminer (v0.4.9) R package). Intrathoracic relapse was defined as any relapse found within the thoracic cavity including mediastinum and parietal pleura but not ribs. Extra-thoracic relapse was defined as any relapse found outside the thoracic cavity, including ribs and axillary, cervical and supraclavicular LNs. To estimate the relapse-site-specific (sub-distribution) HR, the Fine-Gray competing risk regression model was applied using cmprsk (v2.2-11) R package and adjusted for age, stage, pack-years, surgery type and adjuvant therapy. In this analysis, relapses at the specific site (intrathoracic-only or extra-thoracic with or without intrathoracic) were counted as events, and relapses at other sites or non-lung cancer deaths were treated as competing events. Adding sex as a variable in the Cox regression and the Fine-Gray regression models did not change the results (data not shown). Relapsed cases with uncertain sites and/or uncertain origins were excluded from relapse site-specific analysis.

Survival analysis (Memorial Sloan Kettering Cancer Center cohort)

Participant selection. From the Memorial Sloan Kettering Cancer Center Thoracic Surgery Service prospectively maintained database, 712 participants who had undergone surgical resection for pathological stage (TNM staging, version 7) IB to IIIA primary LUAD from January 2006 to December 2014 were identified. Exclusion criteria were: receipt of induction therapy, noninvasive histology and R2 resection classification.

Statistical analysis. The distribution of participant clinicopathological characteristics was summarized as frequencies and percentages for categorical factors or medians, 25th and 75th percentiles for continuous factors. DFS was calculated from the date of surgery to the date of any recurrence or death, whichever occurred first. Participants were otherwise censored on the date of the last follow-up. DFS was estimated using the Kaplan–Meier method and compared between groups using the log-rank test. The relationships between factors of interest (STAS status, necrosis status and the combination of the two) and DFS were quantified using multivariable Cox proportional hazards models, controlling for age at surgery, pathological stage (1, 2 and 3), pack-years, surgery type (sublobar versus lobar or greater) and any adjuvant therapy. All statistical tests were two sided and $P < 0.05$ was considered statistically significant. Analyses were conducted using Stata 15.1 (StataCorp) and R 4.1.2 (R Foundation for Statistical Computing).

Statistical analysis

All statistical tests were performed in R (version 3.6.1 unless otherwise specified). Tests involving correlations were performed using `cor.test` with Spearman's method. Tests involving comparisons of distributions were performed using Wilcoxon rank-sum test, Wilcoxon signed-rank test for paired analysis, or linear mixed-effect regression analysis as stated, using `wilcox.test` function implemented as base package in R, `wilcox.exact` function (exactRankTests (v0.8-34) R package), or `lme` function (nlme (v3.1-155) R package), respectively. Fisher's exact test or Chi-square test were applied for count data as stated, using `fisher.test` or `chisq.test` functions implemented in R. P values were adjusted for multiple comparisons using the BH method using `p.adjust` function implemented in R unless otherwise stated, and reported as q values. All statistical tests were two sided unless otherwise specified. The numbers of data points included in the analysis were annotated in the corresponding figures and/or figure legends. The packages `tidyverse` (v1.3.2), `data.table` (v1.14.2) and `fst` (v0.9.8) were used for data handling in R. Plotting was done using `ggplot2` (v3.3.6), `ComplexHeatmap` (v2.2.0), `RColorBrewer` (v1.1-3), `gridExtra` (v2.3), `ggfittxt` (v0.9.1), `cowplot` (v1.1.1), `ggpubr` (v0.4.0), `ggsci` (v2.9), `gtable` (v0.3.0), `scales` (v1.2.0), `dendsort` (v0.3.4), `seriation` (v1.3.1), `circlize` (v0.4.15), `ggalluvial` (v0.12.3), `ggnewscale` (v0.4.7), `ggeasy` (v0.1.3) and `ggrepel` (v0.9.1) R packages.

Reporting summary

Further information on research design is available in the Nature Portfolio Reporting Summary linked to this article.

Data availability

The WES data and RNA-seq data (in each case from the TRACERx study) used during this study have been deposited at the European Genome-phenome Archive (EGA), which is hosted by The European Bioinformatics Institute (EBI) and the Centre for Genomic Regulation (CRG) under the accession codes [EGAS00001006494](https://www.ebi.ac.uk/ega/studies/EGAS00001006494) (WES) and [EGAS00001006517](https://www.ebi.ac.uk/ega/studies/EGAS00001006517) (RNA-seq); access is controlled by the TRACERx data access committee and details on how to apply for access are available at the linked page. Hallmark gene sets⁵⁸ were downloaded from Molecular Signatures Database (<https://www.gsea-msigdb.org/gsea/msigdb/>).

Code availability

Code used to process data and generate figures is available at <https://doi.org/10.5281/zenodo.7543311>.

References

43. World Health Organization. Classification of Tumours Editorial Board. *Thoracic Tumours: WHO Classification of Tumours*, 5th Edn (2021).
44. Rosenthal, R. et al. Neoantigen-directed immune escape in lung cancer evolution. *Nature* **567**, 479–485 (2019).
45. AbdulJabbar, K. et al. Geospatial immune variability illuminates differential evolution of lung adenocarcinoma. *Nat. Med.* **26**, 1054–1062 (2020).
46. Hendry, S. et al. Assessing tumor-infiltrating lymphocytes in solid tumors: a practical review for pathologists and proposal for a standardized method from the international immuno-oncology biomarkers working group: part 2: TILs in melanoma, gastrointestinal tract carcinomas, non-small cell lung carcinoma and mesothelioma, endometrial and ovarian carcinomas, squamous cell carcinoma of the head and neck, genitourinary carcinomas, and primary brain tumors. *Adv. Anat. Pathol.* **24**, 311–335 (2017).
47. Denkert, C. et al. Standardized evaluation of tumor-infiltrating lymphocytes in breast cancer: results of the ring studies of the international immuno-oncology biomarker working group. *Mod. Pathol.* **29**, 1155–1164 (2016).
48. Van Loo, P. et al. Allele-specific copy number analysis of tumors. *Proc. Natl Acad. Sci. USA* **107**, 16910–16915 (2010).
49. Watkins, T. B. K. et al. Pervasive chromosomal instability and karyotype order in tumour evolution. *Nature* **587**, 126–132 (2020).
50. Roth, A. et al. PyClone: statistical inference of clonal population structure in cancer. *Nat. Methods* **11**, 396–398 (2014).
51. Burrell, R. A. et al. Replication stress links structural and numerical cancer chromosomal instability. *Nature* **494**, 492–496 (2013).
52. Benjamini, Y. & Hochberg, Y. Controlling the false discovery rate: a practical and powerful approach to multiple testing. *J. R. Stat. Soc.* **57**, 289–300 (1995).
53. Ferrer-Bonsoms, J. A., Jareno, L. & Rubio, A. Rediscover: an R package to identify mutually exclusive mutations. *Bioinformatics* <https://doi.org/10.1093/bioinformatics/btab709> (2021).
54. Li, B. & Dewey, C. N. RSEM: accurate transcript quantification from RNA-seq data with or without a reference genome. *BMC Bioinformatics* **12**, 323 (2011).
55. Love, M. I., Huber, W. & Anders, S. Moderated estimation of fold change and dispersion for RNA-seq data with DESeq2. *Genome Biol.* **15**, 550 (2014).
56. Korotkevich, G. et al. Fast gene-set enrichment analysis. Preprint at *bioRxiv* <https://doi.org/10.1101/060012> (2021).
57. Liberzon, A. et al. The Molecular Signatures Database hallmark gene set collection. *Cell Syst.* **1**, 417–425 (2015).
58. Subramanian, A. et al. Gene-set enrichment analysis: a knowledge-based approach for interpreting genome-wide expression profiles. *Proc. Natl Acad. Sci. USA* **102**, 15545–15550 (2005).
59. Hänzelmann, S., Castelo, R. & Guinney, J. GSEA: gene-set variation analysis for microarray and RNA-seq data. *BMC Bioinformatics* **14**, 7 (2013).
60. Kawaguchi, S., Higasa, K., Shimizu, M., Yamada, R. & Matsuda, F. HLA-HD: an accurate HLA typing algorithm for next-generation sequencing data. *Hum. Mutat.* **38**, 788–797 (2017).
61. Reynisson, B., Alvarez, B., Paul, S., Peters, B. & Nielsen, M. NetMHCpan-4.1 and NetMHCIIpan-4.0: improved predictions of MHC antigen presentation by concurrent motif deconvolution and integration of MS MHC eluted ligand data. *Nucleic Acids Res.* **48**, W449–W454 (2020).
62. North, B. V., Curtis, D. & Sham, P. C. A note on the calculation of empirical P values from Monte-Carlo procedures. *Am. J. Hum. Genet.* **71**, 439–441 (2002).
63. Sanchez-Vega, F. et al. Oncogenic signaling pathways in the cancer genome atlas. *Cell* **173**, 321–337 (2018).

Q19

Acknowledgements

The TRACERx study (NCT01888601) is sponsored by University College London (UCL/12/0279) and has been approved by an independent Research Ethics Committee (13/LO/1546). TRACERx is funded by Cancer Research UK (CRUK; C11496/A17786) and coordinated through the CRUK and UCL Cancer Trials Centre, which has a core grant from CRUK (C444/A15953). We gratefully acknowledge the participants and relatives who participated in the TRACERx study. We thank all site personnel, investigators, funders and industry partners that supported the generation of the data within this study. This work was supported by the Francis Crick Institute, which receives its core funding from CRUK (CC2041), the UK Medical Research Council (CC2041) and the Wellcome Trust (CC2041). For the purpose of open access, the author has applied a CC BY public copyright license to any author accepted manuscript version arising from this submission. In particular, we acknowledge the support of Scientific Computing, the Advanced Sequencing Facility and Experimental Histopathology departments at the Francis Crick Institute. This work was also supported by the CRUK Lung Cancer Centre of Excellence and the CRUK City of London Centre Award (C7893/A26233) as well as the UCL Experimental Cancer Medicine Centre. Memorial Sloan Kettering Cancer Center has licensed intellectual property related to mesothelin-targeted chimeric antigen receptors and T cell therapies to ATARA Biotherapeutics, and has associated financial interests. [BioRender.com](https://www.biorender.com) aided in the generation of Fig. 4 and Extended Data Figs. 1k and 6a. T.K. is supported by the JSPS Overseas Research Fellowships Program (202060447). D.A.M. is supported by the CRUK Lung Cancer Centre of Excellence (C11496/A30025). M.A.B. is supported by CRUK, the Rosetrees Trust and the Francis Crick Institute. T.B.K.W. is supported by the Francis Crick Institute, as well as the Marie Curie ITN Project PLOIDYNET (FP7-PEOPLE-2013, 607722), Breast Cancer Research Foundation, Royal Society Research Professorships Enhancement Award (RP/EA/180007) and the Foulkes Foundation. A. Huebner is supported by CRUK. A.M.F. is supported by Stand Up To Cancer (SU2C-AACR-DT23-17). H.Z. is supported by the China Scholarship Council for a 4-year PhD study and the Breast Cancer Research Foundation. F.G.-V. is supported by Generalitat Valenciana fellowships program (APOSTD/2021/168). C.M.-R. is supported by the Rosetrees Trust (M630) and Wellcome Trust. E.C. is supported by CRUK (TRACERx (C11496/A17786)) and the Francis Crick Institute. K.S.S.E. was supported by the European Union's Horizon 2020 research and innovation program under the Marie Skłodowska-Curie grant agreement no. 838540 and the Royal Society (RF\ERE\210216). S.H. is supported by CRUK and the Rosetrees Trust. C.T.H. has received funding from NIHR University College London Hospitals Biomedical Research Centre. S.Z. is a CRUK Career Development Fellow (award ref. RCCCDF-Nov21\100005) and is supported by Rosetrees Trust (grant ref. M917) and CRUK UCL Centre Non-Clinical Training Award (CANTAC721\100022). K.L. is funded by the UK Medical Research Council (MR/P014712/1 and MR/V033077/1), Rosetrees Trust and Cotswold Trust (A2437) and CRUK (C69256/A30194). E.L.C., J.D. and P.V.L. are supported by the Francis Crick Institute, which receives its core funding from CRUK (CC2008), the UK Medical Research Council (CC2008) and the Wellcome Trust (CC2008). P.V.L. is a Winton Group Leader in recognition of the Winton Charitable Foundation's support toward the establishment of the Francis Crick Institute. P.V.L. is a CPRIT Scholar in Cancer Research and acknowledges CPRIT grant support (RR210006). P.S.A.'s laboratory work is supported by grants from the National Institutes of Health (P30 CA008748, R01 CA236615, R01 CA235667 and U01 CA214195), the US Department of Defense (CA180889 and CA200437), the DallePezze Foundation and the Derfner Foundation. P.S.A.'s laboratory receives research support from ATARA Biotherapeutics. D.R.J. is supported by National Institutes of Health grants R01CA217169 and R01CA240472. T.M. is supported by the UK National Institute of Health Research University

College London Hospital Biomedical Research Centre. N.M. is a Sir Henry Dale Fellow, jointly funded by the Wellcome Trust and the Royal Society (grant no. 211179/Z/18/Z) and also receives funding from CRUK, Rosetrees and the National Institute for Health Research (NIHR) Biomedical Research Centre at University College London Hospitals and the CRUK University College London Experimental Cancer Medicine Centre. M.J.-H. is a CRUK Career Establishment Awardee and has received funding from CRUK, IASLC International Lung Cancer Foundation, Lung Cancer Research Foundation, Rosetrees Trust, UKI NETs and NIHR University College London Hospitals Biomedical Research Centre. C.S. is a Royal Society Napier Research Professor (RSRP\R\210001). C.S. is funded by CRUK (TRACERx (C11496/A17786)), PEACE (C416/A21999) and CRUK Cancer Immunotherapy Catalyst Network); CRUK Lung Cancer Centre of Excellence (C11496/A30025); the Rosetrees Trust, Butterfield and Stonegate Trusts; NovoNordisk Foundation (ID16584); Royal Society Professorship Enhancement Award (RP/EA/180007); NIHR University College London Hospitals Biomedical Research Centre; the CRUK University College London Centre; Experimental Cancer Medicine Centre; the Breast Cancer Research Foundation (US); and The Mark Foundation for Cancer Research Aspire Award (grant 21-029-ASP). This work was supported by a Stand Up To Cancer-LUNGevity-American Lung Association Lung Cancer Interception Dream Team Translational Research Grant (grant no. SU2C-AACR-DT23-17 to S. M. Dubinett and A. E. Spira). Stand Up To Cancer is a division of the Entertainment Industry Foundation. Research grants are administered by the American Association for Cancer Research, the Scientific Partner of SU2C. C.S. is in receipt of an ERC Advanced Grant (PROTEUS) from the European Research Council under the European Union's Horizon 2020 research and innovation program (grant agreement no. 835297).

Author contributions

T.K. collated the cohort and clinicopathological data, conducted bioinformatics analyses and wrote the manuscript. D.A.M. led the central pathology review, collated the cohort and pathological data and wrote the manuscript. S.V. led the sample extraction and management and was supported by C.N.-L., A.T. and N.M. S.W. led the genomic sequencing. M.A.B. collated the cohort and clinicopathological data, processed the genomic data and helped write the manuscript. T.B.K.W., K.G., A. Huebner, E.C. and K.S.S.E. processed the genomic data, assisted with bioinformatics analyses and helped write the manuscript. M.S.H., C.P., H.Z., F.G.-V., S.S., N.K., M.D., O.P., E.L.L., C.M.-R., J.R.M.B., D.B., B.B.C. and C.L. processed the genomic data and assisted with bioinformatics analyses. S.H. assisted with clinical annotation and helped write the manuscript. C.T.H. assisted with clinical annotation and data processing. A.M.F. and C.A. processed the genomic and ctDNA data, assisted with bioinformatics analyses and helped write the manuscript. N.J.B., K.L. and S.Z. helped direct bioinformatics and statistical analyses. P.S.A., K.S.T., W.C., F.S.-V., D.R.J., N.R. and W.D.T. analyzed external cohort data and contributed to writing the manuscript. E.L.C., J.D., P.V.L. and T.M. contributed to writing the manuscript. A. Hackshaw helped oversee the running of the TRACERx study. R.S., J.L.Q. and A.G.N. supported central pathology review and helped write the manuscript. M.J.-H., N.M. and C.S. jointly designed and supervised the study and helped write the manuscript. Study design, conduct and clinical and laboratory oversight, M.J.-H., N.M. and C.S. Informatics supervision, N.M., N.J.B., K.L., S.Z. and C.S. Cohort and clinical annotation, T.K., D.A.M., M.A.B., C.A., S.H., C.T.H., M.J.-H., C.S., A. Hackshaw and UCL Cancer Trials Centre. Central pathology review, D.A.M., A.G.N., J.L.Q., R.S., M.A.B. and T.K. Sample extraction and management, S.V., C.N.-L., A.T., N.M. and the EHP STP (Experimental Histopathology Science Technology Platform). Genomic sequencing, S.W. and the ASF STP (Advanced Sequencing Facility Science Technology Platform). Cohort overview, T.K., D.A.M. and M.D. Genetic alteration and evolutionary dependency,

Q16

Q17

T.K., K.G., A.M.F., T.B.K.W., E.L.L., M.S.H., C.P., H.Z., B.B.C., S.Z. and N.M. Transcriptomic data analysis, T.K., C.M.-R., J.R.M.B., C.P., D.B., F.G.-V., S.S., N.K. and N.M. Metastasis data analysis, T.K., A. Huebner and M.A.B. ctDNA data analysis, C.A., A.M.F., T.K., N.J.B. and C.S. Tumor immune microenvironment analysis, T.K., C.P., O.P., C.P., C.L., K.G., E.C., K.S.S.E., C.T.H., N.M. and C.S. Regression analysis, survival analysis and statistics, T.K., M.S.H., A.M.F., K.L. and A. Hackshaw. External cohort data analysis. P.S.A., K.S.T., W.C., F.S.-V., D.R.J., N.R. and W.D.T. Manuscript writing, D.A.M., T.K., M.A.B., T.B.K.W., A.M.F., K.G., A. Huebner, E.C., K.S.S.E., E.L.C., J.D., P.V.L., F.S.-V., P.S.A., K.S.T., W.C., D.R.J., N.R., W.D.T., T.M., R.S., J.L.Q., A.G.N., N.M., M.J.-H. and C.S.

Competing interests

D.A.M. reports speaker fees from AstraZeneca, Eli Lilly and Takeda, consultancy fees from AstraZeneca, Thermo Fisher, Takeda, Amgen, Janssen, MIM Software, Bristol Myers Squibb (BMS) and Eli Lilly and has received educational support from Takeda and Amgen. S.V. is a co-inventor to a patent for detecting molecules in a sample patent no. 10578620. M.A.B. has consulted for Achilles Therapeutics. D.B. reports personal fees from NanoString and AstraZeneca, and has a patent PCT/GB2020/050221 issued on methods for cancer prognostication. K.S.S.E. received research grant funding from BMS. C.T.H. has received speaker fees from AstraZeneca. K.L. has a patent on indel burden and CPI response pending and speaker fees from Roche tissue diagnostics, research funding from CRUK TDL/Ono/LifeArc alliance, Genesis Therapeutics, and consulting roles with Monopteros Therapeutics and Kynos Therapeutics. N.J.B. is a co-inventor to a patent for identification of responders to cancer treatment (PCT/GB2018/051912). E.L.C. is employed by and holds shares in Achilles Therapeutics. P.S.A. is a Scientific Advisory Board Member and Consultant for ATARA Biotherapeutics, Bayer, Carisma Therapeutics, Imugene, ImmPactBio, Johnston & Johnston, Orion and OutpaceBio; declares patents, royalties and intellectual property on mesothelin-targeted CARs and other T cell therapies, which have been licensed to ATARA Biotherapeutics, issued patent method for detection of cancer cells using virus, and pending patent applications on PD-1 dominant negative receptor, wireless pulse-oximetry device, and on an ex vivo malignant pleural effusion culture system. D.R.J. has consulted for AstraZeneca and is a member of the Clinical Trial Steering Committee for Merck. N.R. serves on an NCI Thoracic Malignancies Steering Committee (which is a compensated role). W.D.T. is a non-paid consultant for the LCMC3 and LCMC4 neoadjuvant clinical trials. A. Hackshaw has received fees for being a member of Independent Data Monitoring Committees for Roche-sponsored clinical trials, and academic projects coordinated by Roche. R.S. reports nonfinancial support from Merck and BMS, research support from Merck, Puma Biotechnology and Roche, and personal fees from Roche, BMS and Exact Sciences for advisory boards. A.G.N. reports personal fees from Merck, Boehringer Ingelheim, Novartis, AstraZeneca, BMS, Roche, Abbvie, Oncologica, Uptodate, European Society of Oncology, Takeda UK and Liberium, and personal fees and grants from Pfizer. N.M. has stock options in and has consulted for Achilles Therapeutics and holds a European patent in determining HLA LOH (PCT/GB2018/052004) and is a co-inventor to a patent for identification of responders to cancer treatment (PCT/GB2018/051912). M.J.-H. has consulted for and is a member of the Scientific Advisory Board and Steering Committee

for Achilles Therapeutics, has received speaker honoraria from Pfizer, Astex Pharmaceuticals and Oslo Cancer Cluster, and holds a patent PCT/US2017/028013 relating to methods for lung cancer detection. C.A. has received speaking honoraria or expenses from AstraZeneca and BMS and reports employment at AstraZeneca. C.A. and C.S. are inventors on a European patent application relating to assay technology to detect tumor recurrence (PCT/GB2017/053289), and the patent has been licensed to commercial entities and, under their terms of employment, C.A. and C.S. are due a revenue share of any revenue generated from such license(s). C.A. and C.S. declare a patent application (PCT/US2017/028013) for methods to detect lung cancer. A.M.F., C.A. and C.S. are named inventors on a patent application to determine methods and systems for tumor monitoring (PCT/EP2022/077987). C.S. acknowledges grant support from AstraZeneca, Boehringer Ingelheim, BMS, Pfizer, Roche-Ventana, Invitae (previously Archer Dx—collaboration in minimal residual disease sequencing technologies) and Ono Pharmaceutical. C.S. is an AstraZeneca Advisory Board member and Chief Investigator for the AZ MeRmaid 1 and 2 clinical trials and is also co-chief investigator of the NHS Galleri trial funded by GRAIL and a paid member of GRAIL's Scientific Advisory Board. C.S. receives consultant fees from Achilles Therapeutics (also SAB member), Bicycle Therapeutics (also a SAB member), Genentech, Medicxi, Roche Innovation Centre – Shanghai, Metabomed (until July 2022) and the Sarah Cannon Research Institute. C.S. had stock options in Apogen Biotechnologies and GRAIL until June 2021, and currently has stock options in Epic Bioscience, Bicycle Therapeutics, and has stock options in and is co-founder of Achilles Therapeutics. C.S. holds patents relating to targeting neoantigens (PCT/EP2016/059401), identifying patient response to immune checkpoint blockade (PCT/EP2016/071471), determining HLA LOH (PCT/GB2018/052004), predicting survival rates of patients with cancer (PCT/GB2020/050221), identifying patients who respond to cancer treatment (PCT/GB2018/051912), methods for lung cancer detection (US20190106751A1) and both a European and US patent related to identifying insertion/deletion mutation targets (PCT/GB2018/051892). The remaining authors declare no competing interests.

Q18

Additional information

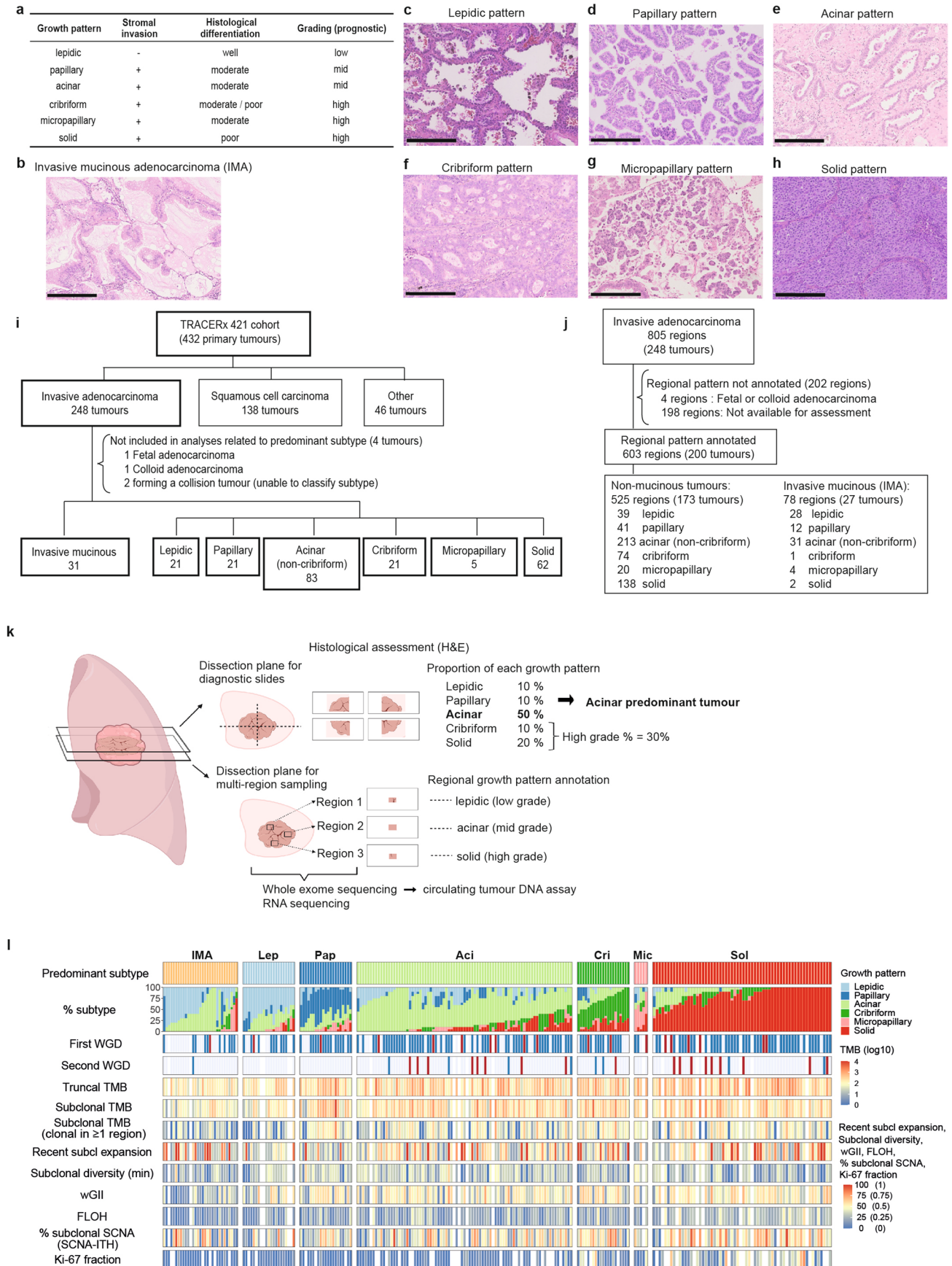
Extended data is available for this paper at <https://doi.org/10.1038/s41591-023-02230-w>.

Supplementary information The online version contains supplementary material available at <https://doi.org/10.1038/s41591-023-02230-w>.

Correspondence and requests for materials should be addressed to Nicholas McGranahan, Charles Swanton or Mariam Jamal-Hanjani.

Peer review information *Nature Medicine* thanks Timothy Chan and the other, anonymous, reviewer(s) for their contribution to the peer review of this work. Primary Handling Editor: Joao Monteiro, in collaboration with the *Nature Medicine* team.

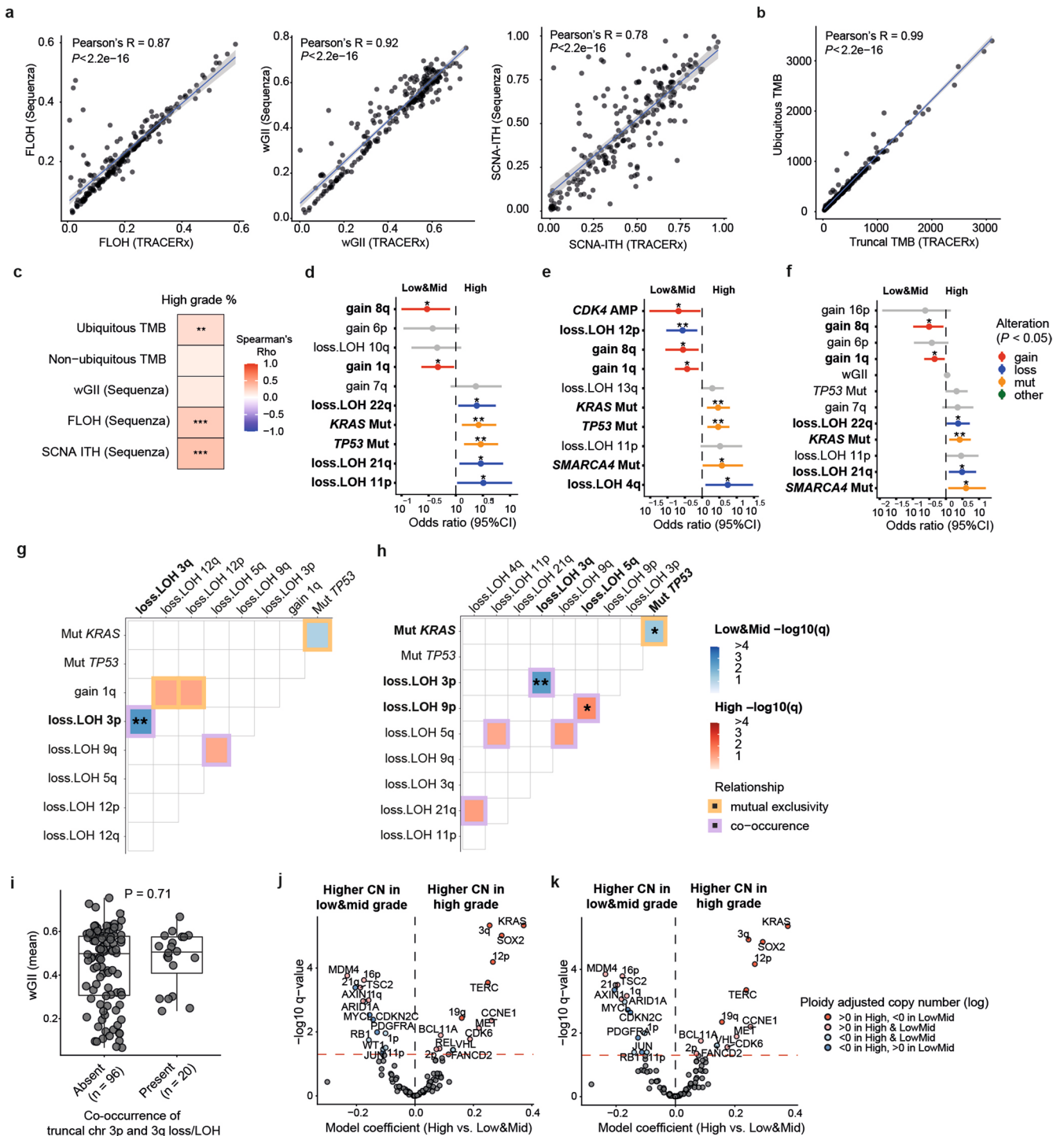
Reprints and permissions information is available at www.nature.com/reprints.



Extended Data Fig. 1 | See next page for caption.

Extended Data Fig. 1 | Histopathological assessment of the TRACERx 421 LUAD cohort. **a.** Definition and categorisation of LUAD growth patterns. **b.** Representative haematoxylin and eosin (H&E) photo of invasive mucinous adenocarcinoma (IMA). **c-h.** Representative H&E photos of lepidic (**c**), papillary (**d**), acinar (**e**), cribriform (**f**), micropapillary (**g**), and solid (**h**) pattern observed in LUAD. Scale bar, 250 μ m. **i.** Number of tumours by histological entity in the TRACERx 421 cohort and further annotation of the number of LUAD tumours by predominant subtype. **j.** Number of regions with growth pattern assessment. **k.** Schematic of histological assessment in the TRACERx study. Proportions of each subtype in the diagnostic slides were reported, and the predominant subtype was used to label each tumour. Multi-region sampling specimens were

processed for whole exome and RNA sequencing, and each region was annotated with the representative growth pattern. **l.** Overview of TRACERx 421 LUAD cohort. Fetal adenocarcinoma, colloid adenocarcinoma, and two tumours from a collision tumour determined by genomic analysis were not included in the plot ($n = 244$ tumours in 240 patients are shown). Each column represents one tumour. The proportion of each growth pattern (subtype) based on diagnostic sectional area, genomic variables, and Ki-67 fraction by immunohistochemical staining are summarised. Missing data are shown in grey. WGD, whole genome doubling; TMB, tumour mutational burden; wGII, weighted genome instability index; FLOH, fraction of the genome subject to loss of heterozygosity; SCNA, somatic copy number alteration; ITH, intra-tumour heterogeneity.

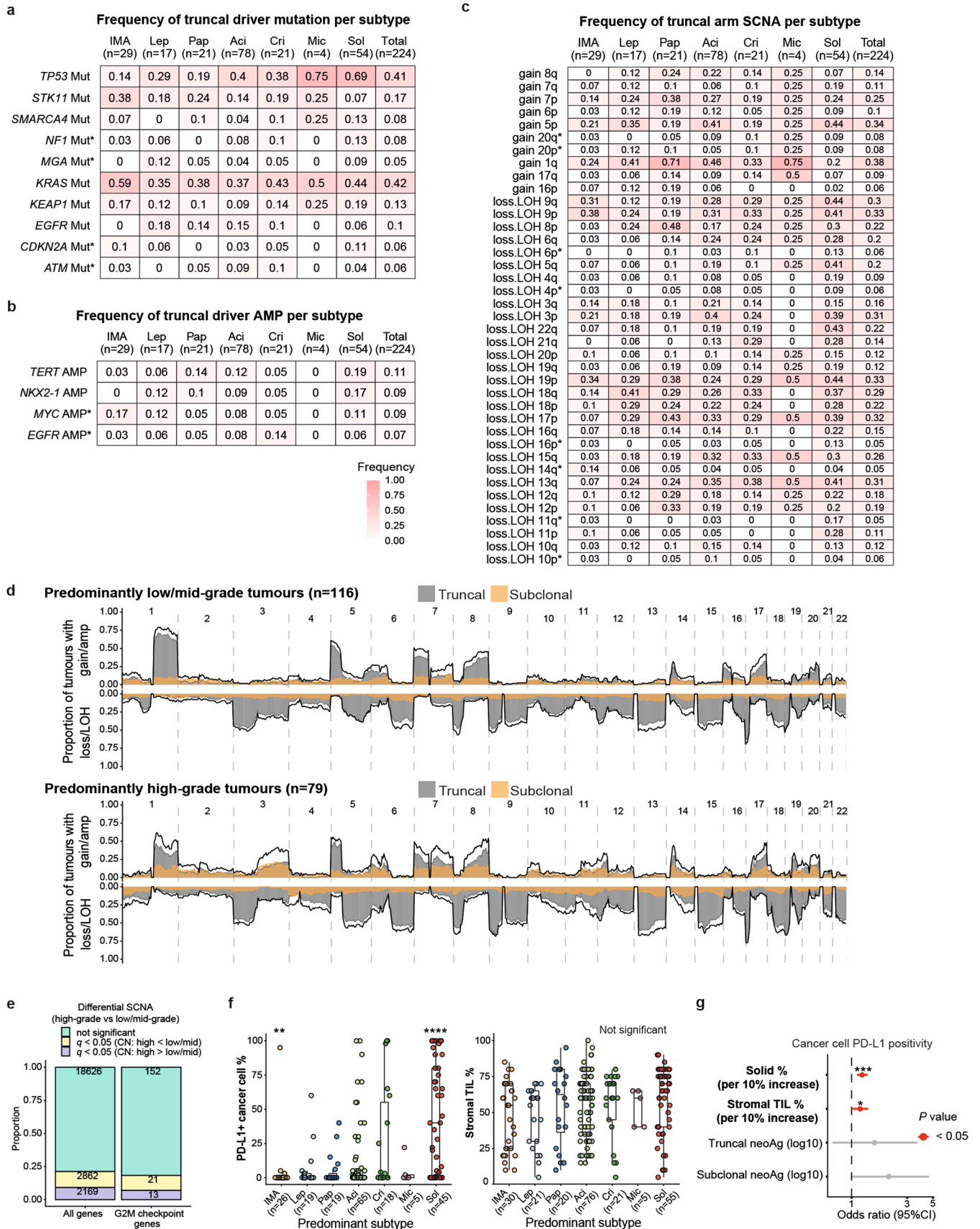


Extended Data Fig. 2 | See next page for caption.

Extended Data Fig. 2 | Validation of SCNA analysis using orthogonal methods.

a, b. Comparison of intra-tumour heterogeneity (ITH) metrics calculated using TRACERx analytical pipeline vs orthogonal methods. **(a)** Comparison of the mean fraction of the genome subject to loss of heterozygosity (FLOH), mean weighted genome instability index (wGII), and somatic copy number alteration ITH (SCNA-ITH) by SCNA profiles generated by the TRACERx pipeline (based on ASCAT⁴³ with additional multi-sample SCNA estimation approach^{9,44}) against SCNA profiles generated by Sequenza¹² ($n = 223$ tumours) and **(b)** a comparison of truncal tumour mutational burden (TMB) using the TRACERx pipeline (clonality inferred by the modified version of PyClone⁴⁵) vs ubiquitous TMB ($n = 224$ tumours). Blue lines and grey bands represent linear regression lines with 95% confidence intervals (CIs). Pearson's correlation coefficient and P value are shown. **c.** Correlation of genomic variables calculated using orthogonal methods and the proportion of high-grade patterns within each tumour. Colour scale reflects Spearman's rank correlation coefficient (ρ). Correlation P values were corrected for multiple testing according to Benjamini-Hochberg (BH) and asterisks indicate q value ranges * $q < 0.05$, ** $q < 0.01$, *** $q < 0.001$, **** $q < 0.0001$. **d-f.** Adjusted odds ratios with 95% CIs of truncal genomic alterations associated with the predominance of high-grade ($n = 79$ tumours) or low-/mid-grade patterns ($n = 116$ tumours). Genomic alterations selected by the model simplification are shown when **(d)** truncal alterations observed in more than 10% of the tumours in the cohort are included in the analysis, or when **(e)** SCNA profiles generated by Sequenza¹² are used, or when **(f)** wGII is added to the model shown in Fig. 1d. Asterisks indicate type II ANOVA P value ranges * $P < 0.05$, ** $P < 0.01$, *** $P < 0.001$. Colour represents the type of genomic

alteration. Statistically significant alterations ($P < 0.05$) are indicated in bold. **g-h.** Mutual exclusivity and co-occurrence of truncal driver gene alterations and chromosome arm SCNAs specific to either predominantly high-grade or low/mid-grade tumours when **(g)** truncal alterations observed in more than 10% of the tumours in the cohort are included in the analysis, or when **(h)** SCNA profiles generated by Sequenza¹² are used. Truncal alterations with unadjusted $P < 0.05$ for both predominantly high- and low/mid-grade tumours are filtered out. Colour of the edge represents the relationship (mutual exclusivity vs co-occurrence) and the negative log of the q value (BH method) is represented in blue colour scale in predominantly low/mid-grade tumours and red colour scale in predominantly high-grade tumours. Relationships with $q < 0.1$ are shown and asterisks indicate q value ranges * $q < 0.05$, ** $q < 0.01$. Covariates in statistically significant relationships ($q < 0.05$) are indicated in bold. **i.** Comparison of mean wGII between tumours with ($n = 20$) and without ($n = 96$) co-occurrence of truncal loss/LOH of chromosome 3p and 3q in predominantly low/mid-grade tumours. P value was calculated using a two-sided Wilcoxon rank-sum test. **j-k.** Comparison of ploidy adjusted mean copy number of chromosomal arm and driver genes between high-grade and low/mid-grade predominant tumours, **(j)** using SCNA profiles generated by Sequenza¹², and **(k)** adding wGII to the regression model. Fixed effect coefficients of the linear mixed effect model with tumour as a random effect are displayed on the x-axis, and the negative log of the q value (BH method) is displayed on the y-axis. Colour represents the sign or the mean ploidy adjusted copy number, stratified with high-grade and low/mid-grade predominance. Data points with q value ≥ 0.05 are coloured in grey. Horizontal red dashed line represents $q = 0.05$.



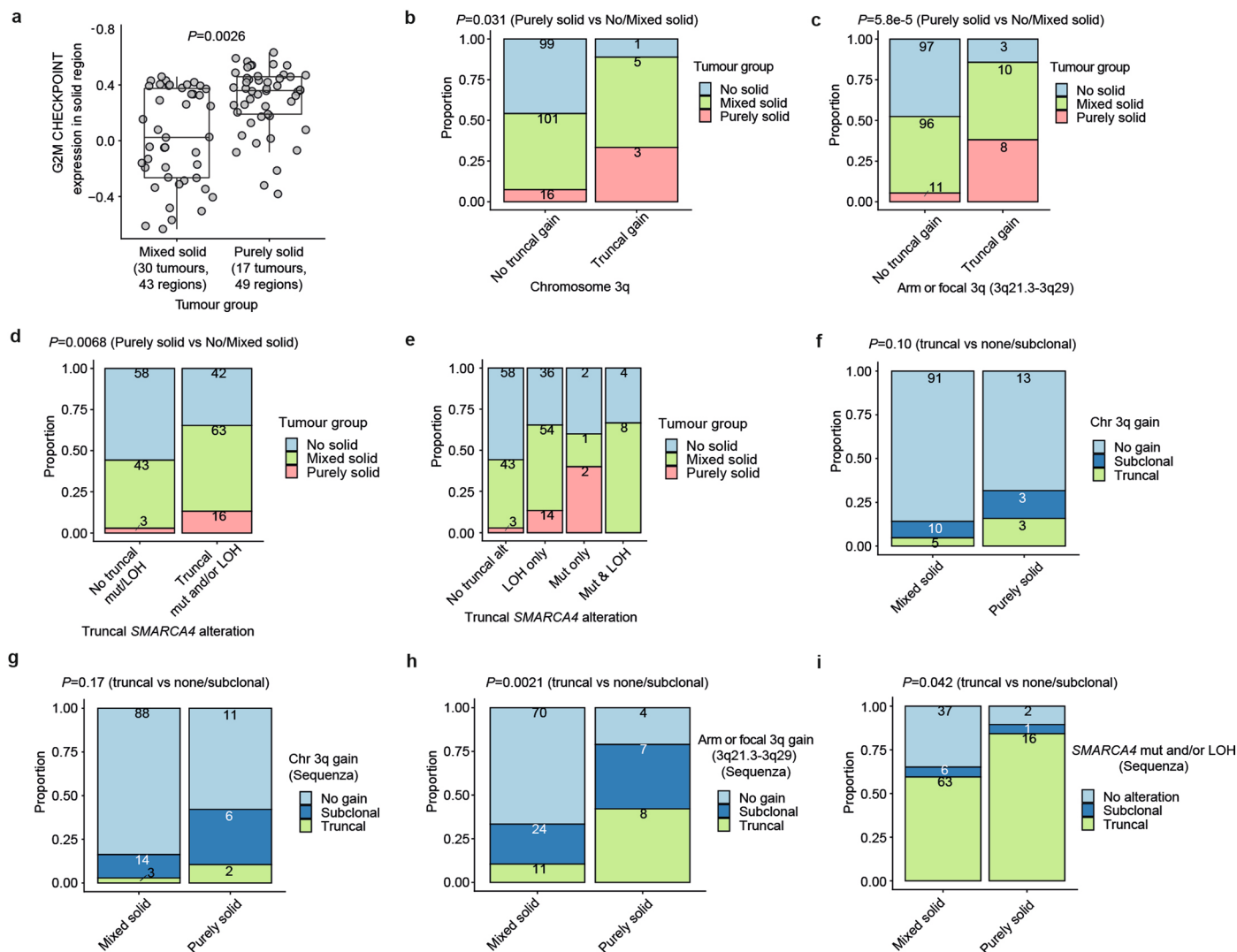
Extended Data Fig. 3 | See next page for caption.

Extended Data Fig. 3 | Genomic correlates of LUAD predominant subtypes. **a–c.** Frequency of **(a)** truncal driver mutations, **(b)** truncal driver gene amplifications, and **(c)** truncal chromosomal arm level SCNAs (gain/loss&LOH) in LUAD predominant subtypes. Recurrent truncal alterations observed in more than 5% of the tumours in the cohort are shown. Asterisks represent the alterations observed in fewer than 10 tumours in both predominantly high- and low/mid-grade predominant tumours. Colour scale represents the frequency of the alteration observed within each subtype. Tumours with multi-region SCNA data were included in the analysis ($n = 224$). **d.** Across-genome plots showing the frequency of truncal and subclonal SCNAs of low/mid-grade predominant tumours (**top**) and high-grade predominant tumours (**bottom**). Within each tumour type, the proportion of patients with gains or amplifications (top) and loss/LOH events (bottom) for each chromosome are described. The black line indicates the total (namely the sum of truncal and subclonal) proportion of tumours with SCNAs; the yellow and grey lines or shades indicate the proportion of tumours with subclonal and truncal gains, respectively. **e.** Number of genes with differential SCNA between high-grade and low/mid-grade predominant

tumours. Significantly increased copy number in high-grade predominant tumours compared with low/mid-grade predominant tumours: G2M checkpoint genes, 13/186; all genes, 2169/23657 ($P = 0.36$, chi-square test). **f.** Comparison of **(left)** PD-L1 expression on cancer cells measured by immunohistochemistry ($n = 197$ tumours) and **(right)** stromal tumour infiltrating lymphocyte (TIL) scores ($n = 228$ tumours) across LUAD predominant subtypes. Each predominant subtype was compared against all other subtype tumours. P values were calculated using two-sided Wilcoxon rank sum test and corrected for multiple testing according to Benjamini-Hochberg method. Asterisks indicate q value ranges ** $q < 0.01$, **** $q < 0.0001$. Centre line, median; box limits, upper and lower quartiles; whiskers, 1.5 \times interquartile range. **g.** Adjusted odds ratios with 95% confidence intervals (CIs) for cancer cell PD-L1 positivity ($\geq 1\%$) per tumour estimated by multivariable logistic regression model (PD-L1 positive, $n = 75$ tumours; PD-L1 negative, $n = 102$ tumours). Asterisks indicate type II ANOVA P value ranges * $P < 0.05$, *** $P < 0.001$. Statistically significant ($P < 0.05$) covariates are indicated in bold.

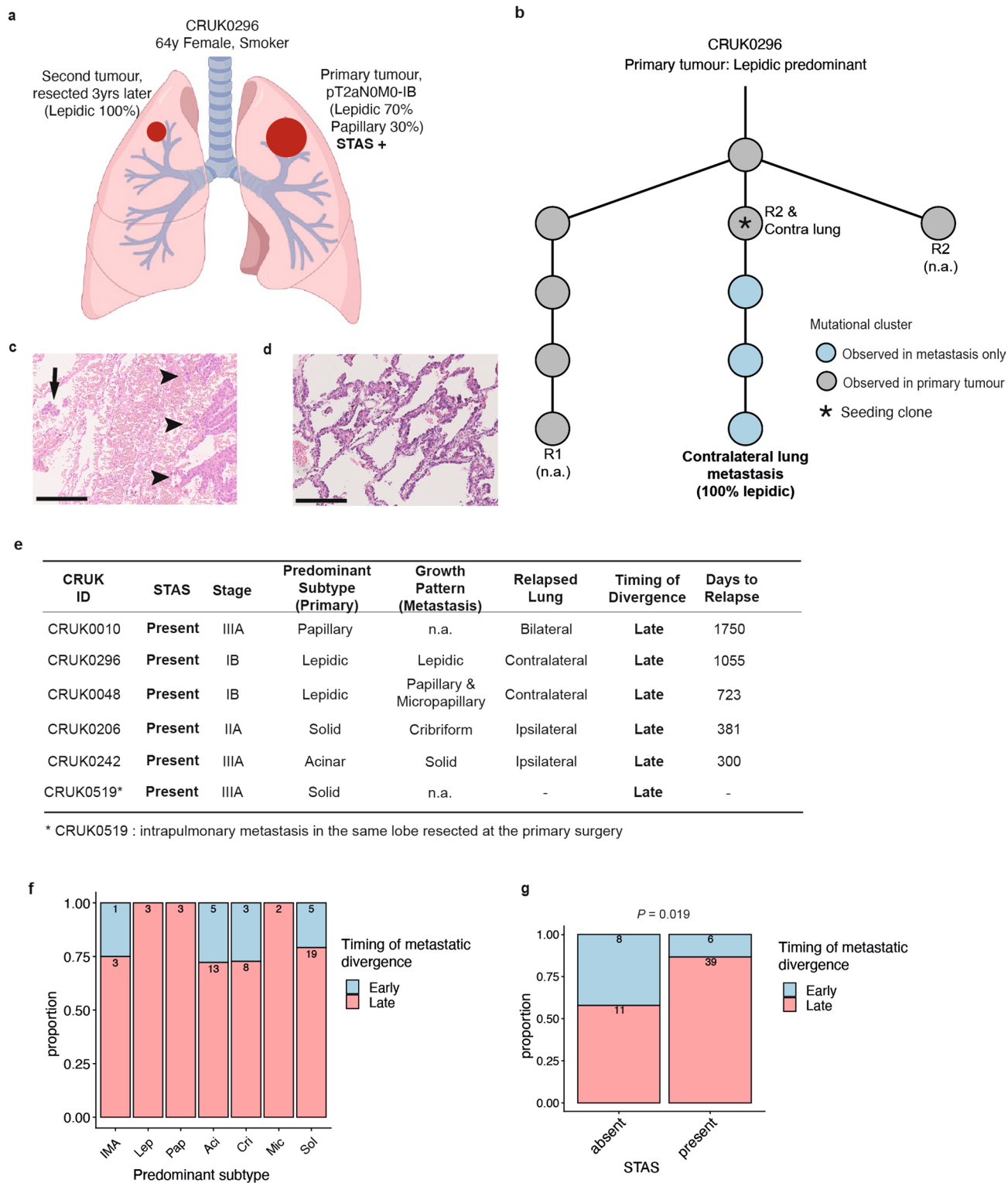
Extended Data Fig. 4 | Morphological intra-tumoural heterogeneity reflects genomic heterogeneity. a-c. Genomic distance between regions calculated by (a) LOH detected by Sequenza (n = 53 tumours) and genomic distance calculated by (b) mutation and (c) LOH only including tumour regions with purity ≥ 0.4 (n = 30 tumours). Each point represents a distance between a pair of regions in a tumour. Tumours containing both different subtype pair(s) and same subtype pair(s) are included in the analysis. Centre line, median; box limits, upper and lower quartiles; whiskers, 1.5 \times interquartile range. *P* values were calculated using a linear mixed effects model, with tumour as a random effect. **d.** Comparison of tumour mutational burden (TMB) between ancestor-like and descendant-like regions (151 regional pairs in 54 tumours). Each line represents an ancestor-descendant-like regional pair. Each point represents one region and the plotted points were duplicated for regions associated with multiple ancestor-descendant-like pairs within a tumour. To assess the mutational burden shared in the majority of the cancer cells in the region, mutations with estimated cancer cell fraction $\geq 95\%$ were counted (TMB CCF95). Enrichment of higher TMB in descendant-like regions compared with the paired ancestor-like regions was evaluated by permutation test (1000 permutations, randomising TMB within each tumour, Monte-Carlo procedure). **e.** Comparison of growth

pattern by grades (**left**) and by the six growth patterns (**right**) between inferred ancestral-like and descendant-like regions. Tumours with single grades are included in the analysis. Colour represents the transition of grade from ancestral-like to descendant-like region. Enrichment of lower-to-higher grade transition (upward transition) was evaluated using a permutation test (1000 permutations, randomising growth patterns within each tumour, Monte-Carlo procedure). **f.** Comparison of regional growth pattern grade in ancestor-descendant-like pairs, inferred by various cutoffs of private loss of heterozygosity (LOH) branch length proportion. All combinations of cutoff for ancestor-like and descendant-like inference shown in the figure yielded empirical *P* value < 0.05 (1000 permutations, Monte-Carlo procedure) when the enrichment of lower-to-higher grade transition (upward transition) was tested. *P* values were not adjusted for the multiple comparisons shown in this panel. **g-h.** Comparison of regional pattern grade in ancestor-descendant-like pairs, inferred by (g) LOH profile generated by Sequenza¹² and (h) both LOH profile and mutational profile (CCF $\geq 95\%$). Enrichment of lower-to-higher grade transition (upward transition) was evaluated using a permutation test (1000 permutations, randomising growth patterns within each tumour, Monte-Carlo procedure).



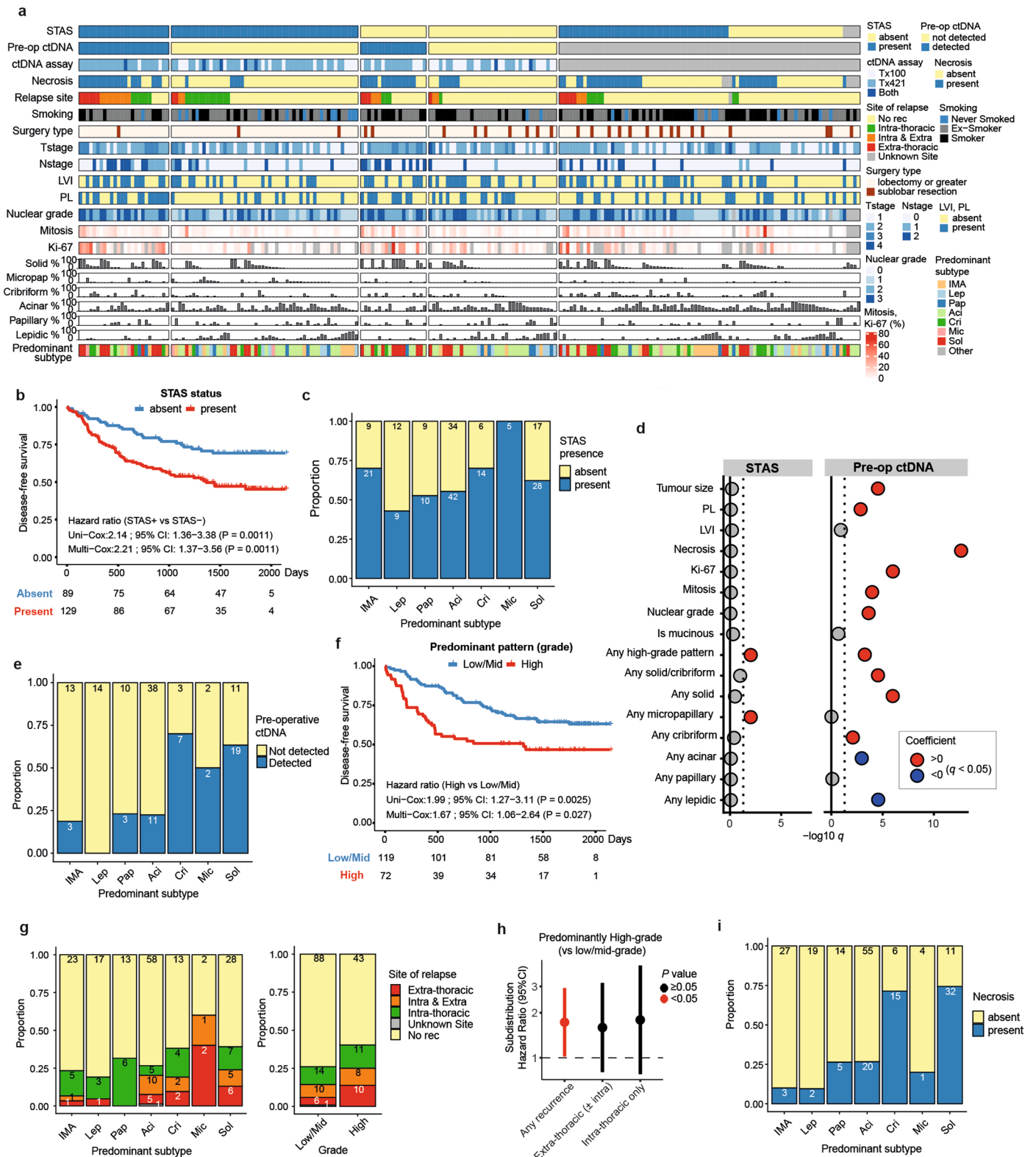
Extended Data Fig. 5 | Characterisation of purely (homogeneously) solid tumours. **a.** Comparison of G2M checkpoint gene expression in solid-pattern regions within purely solid tumours and mixed pattern tumours as defined by both diagnostic and regional growth pattern assessment. Centre line, median; box limits, upper and lower quartiles; whiskers, 1.5× interquartile range. *P* value was calculated using a linear mixed effects model, with tumour as a random effect. **b-e.** Proportion of tumours which are purely solid, mixed pattern with solid component, and without any solid component, compared between tumours with and without **(b)** truncal gain of chromosome arm 3q, **(c)** truncal gain of arm or focal 3q (3q21.3-3q29), **(d)** truncal SMARCA4 mutation and/or

loss of heterozygosity (LOH), and **(e)** compared across the tumours stratified by truncal SMARCA4 mutation and LOH status. *P* value was calculated using a two-sided Fisher’s exact test. **f.** Comparison of the frequency of truncal copy number gain of chromosome arm 3q between mixed pattern tumours with solid component and purely solid tumours. A two-sided Fisher’s exact test was used. **g-i.** Comparison of the frequency of **(g)** copy number gain of chromosome arm 3q, **(h)** gain of arm or focal 3q (3q21.3-3q29), and **(i)** SMARCA4 mutation and/or LOH between mixed pattern tumours with solid component and purely solid tumours using somatic copy number alteration profiles generated by Sequenza. A two-sided Fisher’s exact test was used.



Extended Data Fig. 6 | Analysis of morphology and genomics in metastasis samples. a. Schematic of primary and secondary lung tumours in CRUK0296. Phylogenetic analysis confirmed the contralateral lung lesion to be a metastasis from the primary tumour resected three years earlier. Tumour spread through air spaces (STAS) was positive in the primary tumour. **b.** Phylogenetic tree of a case having lung metastasis with pure lepidic appearance (CRUK0296). Blue nodes are mutation clusters found only in metastasis and grey nodes represent mutation clusters found in the primary tumour. Regional growth pattern is indicated in brackets; n.a., not available; R, region. **c.** Representative haematoxylin and eosin (H&E) slide of a primary tumour of CRUK0296 showing

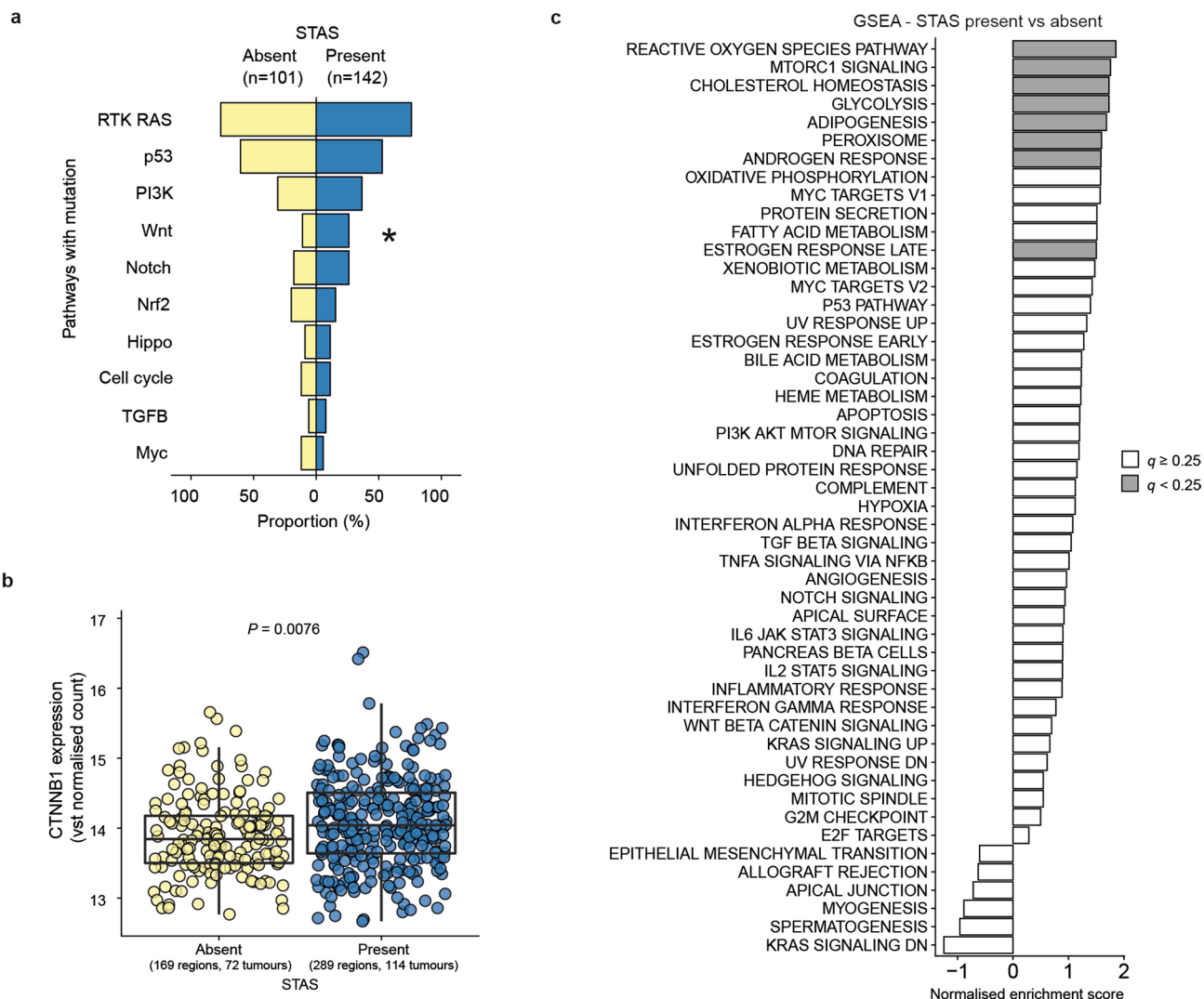
tumour border (arrowheads) and STAS (arrow). **d.** Representative H&E slide of metastasis tumour in the contralateral lung of CRUK0296, which showed a pure lepidic pattern. **e.** Characteristics of five patients having lung recurrence samples sequenced and one patient having an intrapulmonary metastasis resected and sequenced at the time of primary surgery. All six patients showed positive STAS in the primary tumours and phylogenetic analysis revealed late metastatic divergence; n.a., not available. **f.** Proportion of the timing of seeding clone divergence across predominant subtypes of primary tumours. **g.** Frequency of late or early divergence of the metastatic clone compared between tumours with and without STAS. A two-sided Fisher's exact test was used.



Extended Data Fig. 7 | See next page for caption.

Extended Data Fig. 7 | Characterisation of tumours with STAS and preoperative ctDNA shedding. **a.** Overview of the TRACERx 421 LUAD cohort, ordered by the positivity of STAS, pre-operative ctDNA detection, and the site of the relapse (n = 223 patients). Patients with synchronous primary lung cancers were excluded. Colloid and fetal adenocarcinomas are included (predominant subtype = Other). Each column represents each patient. IMA, invasive mucinous adenocarcinoma; LVI, lymphovascular invasion; PL, pleural invasion. Tumours that did not relapse before death or the development of a new primary cancer are treated as no recurrence (No rec). **b.** Kaplan-Meier curve of disease-free survival, comparing STAS present vs absent. Numbers at risk are described at the bottom. Unadjusted and adjusted hazard ratio (HR) (adjusted for age, pathological stage, smoking pack-years, surgery type, and receipt of adjuvant therapy) are shown. **c.** STAS positivity across predominant subtypes of the primary tumour. **d.** Histopathological features associated with STAS positivity (**left**) and pre-operative ctDNA detection (**right**). Negative log of the *q* values (Benjamini-Hochberg method) obtained by multiple univariable logistic regression analyses are presented. Vertical dotted lines represent $q = 0.05$, and variables with

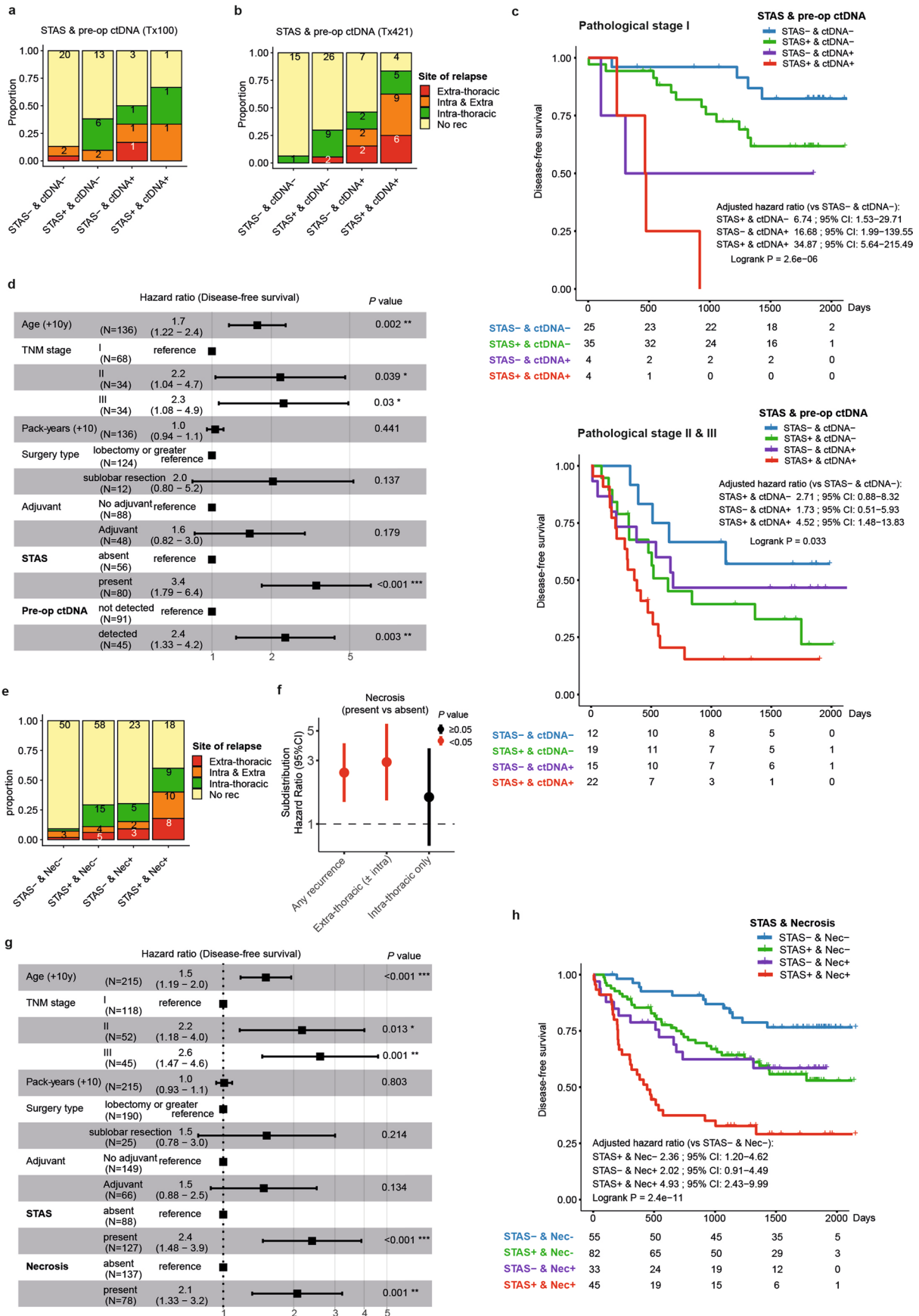
$q < 0.05$ are presented in points with colours which represent the direction of the correlation. **e.** Pre-operative ctDNA positivity across predominant subtypes of the primary tumour. **f.** Kaplan-Meier curve of disease-free survival, comparing patients with predominantly high-grade tumours vs low/mid-grade tumours. Numbers at risk are described at the bottom. Unadjusted and adjusted HR (adjusted for age, stage, pack-years, surgery type, and adjuvant therapy) are shown. **g.** Frequency of the relapse site (intra- and/or extra-thoracic) across predominant subtypes (**left**) and grades of the predominant subtype (**right**) of primary tumour. Tumours that did not relapse before death or the development of a new primary cancer are treated as no recurrence (No rec). **h.** Relapse-site specific (sub-distribution) hazard ratios for predominantly high-grade tumours compared with low/mid-grade tumours, adjusted for age, stage, pack-years, surgery type, and adjuvant therapy, are presented with 95% confidence intervals (CIs) on a logarithmic scale (n = 185 patients). Patients with synchronous primary lung cancers or uncertain site of relapse were excluded from the analysis. $P < 0.05$ are described in red. No corrections were made for multiple comparisons. **i.** Positivity of necrosis across predominant subtypes of the primary tumour.



Extended Data Fig. 8 | Genomic and transcriptomic analyses of STAS in LUAD.

a. Frequency of driver mutations in 10 canonical oncogenic signalling pathways⁶³ in STAS present and absent tumours. P values calculated by two-sided Fisher's exact test were corrected for multiple testing according to Benjamini-Hochberg (BH) method and the asterisk indicates q value range $*q < 0.05$. **b.** Comparison of *CTNNB1* gene expression (variance stabilisation normalised count) between STAS absent ($n = 72$ tumours) and present tumours ($n = 114$ tumours). Each point represents a tumour region (STAS absent, $n = 169$ regions; present, $n = 289$

regions). Centre line, median; box limits, upper and lower quartiles; whiskers, $1.5 \times$ interquartile range. P value was calculated using a linear mixed effect model, with tumour as a random effect. **c.** Gene set enrichment analysis (GSEA) of Hallmark gene sets between STAS absent ($n = 72$ tumours) and present tumours ($n = 112$ tumours). Normalised enrichment score is displayed on the x-axis and indicates the enrichment for a given gene set. Gene sets with $q < 0.25$ (BH method) are described in grey.



Extended Data Fig. 9 | See next page for caption.

Extended Data Fig. 9 | Impact of STAS, pre-operative ctDNA positivity, and necrosis upon site and risk of recurrence. **a, b.** Frequency of the relapse site (intra- and/or extra-thoracic), stratified by the positivity of STAS and pre-operative ctDNA detection. Pre-operative ctDNA data were based on **(a)** the assay previously reported by Abbosh et. al.⁸ (Tx100 cohort) and **(b)** the assay reported in our companion manuscript²⁸ (Tx421 cohort), including 7 patients who underwent both assays in each cohort. Tumours that did not relapse before death or the development of a new primary cancer are treated as no recurrence (No rec). **c.** Kaplan–Meier (KM) curves of disease-free survival, stratified by the positivity of STAS and pre-operative ctDNA detection in **(top)** stage I patients and **(bottom)** stage II & III patients. HRs were adjusted for age, pathological stage, smoking pack-years, and receipt of adjuvant therapy. Surgery type was also added as a covariate for stage I patients but not for stage II & III patients, because only 1 patient underwent sublobar resection in stage II & III patients. Numbers at risk are described below the KM curves. **d.** Positivity of STAS and pre-operative ctDNA detection are incorporated with other tumour and clinical characteristics

in a multivariable Cox proportional hazards model (disease-free survival). Hazard ratios (HRs) of each variable with 95% confidence intervals (CIs) are shown on the horizontal axis. **e.** Frequency of the relapse site (intra- and/or extra-thoracic), stratified by the presence of STAS and necrosis in all LUADs. **f.** Relapse-site specific (subdistribution) HR for positivity of necrosis, adjusted for age, stage, pack-years, surgery type, and adjuvant therapy, are presented with 95% confidence intervals (CIs) on a logarithmic scale ($n = 211$ patients). Patients with synchronous primary lung cancers or uncertain site of relapse were excluded from the analysis. $P < 0.05$ are shown in red. No corrections were made for multiple comparisons. **g.** Positivity of STAS and necrosis are incorporated with other tumour and clinical characteristics in a multivariable Cox proportional hazards model for disease-free survival. HRs of each variable with 95% CIs are shown. **h.** KM curve of disease-free survival, stratified by the positivity of STAS and the presence of necrosis. HRs were adjusted for age, stage, pack-years, surgery type, and adjuvant therapy. Numbers at risk are described at the bottom.

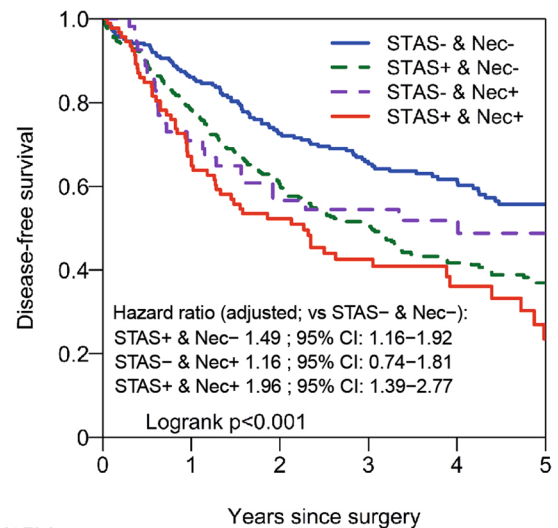
a Summary of patient demographics and clinical characteristics (N=712)

Age	69.5 (IQR 62.8, 76.1)
Pack-years (N=710)	30.0 (IQR 8.0, 50.0)
Type of Surgery	
Pneumonectomy	14 (2.0%)
Bilobectomy	18 (2.5%)
Lobectomy	529 (74%)
Segmentectomy	67 (9.4%)
Wedge resection	84 (12%)
Adjuvant treatment	
None	406 (57%)
Given (any)	274 (38%)
Unknown	32 (4.5%)
pTNM stage (version 7)	
stage I	338 (47%)
stage II	226 (32%)
stage III	148 (21%)
Predominant subtype	
Lepidic	36 (5.1%)
Acinar	311 (44%)
Papillary	85 (12%)
Micropapillary	63 (8.8%)
Solid	199 (28%)
Invasive mucinous adenocarcinoma	14 (2.0%)
Colloid	4 (0.6%)
STAS	
Absent	282 (40%)
Present	430 (60%)
Necrosis	
Absent	562 (79%)
Present	150 (21%)

b Multivariable Cox model for DFS

Variables	Hazard ratio [95% CI]	P value
Age	1.02 [1.01-1.03]	0.0002
pTNM stage (vs stage I)		
stage II	2.26 [1.7-3.01]	<0.0001
stage III	3.44 [2.43-4.88]	<0.0001
Pack-years	1.01 [1-1.01]	0.004
Surgery type (vs lobectomy or greater)		
Sublobar (wedge or segmentectomy)	1.48 [1.14-1.93]	0.003
Adjuvant treatment (vs none)		
Given	0.6 [0.44-0.8]	0.001
Unknown	1.74 [1.08-2.81]	0.023
STAS (vs absent)		
present	1.53 [1.22-1.92]	0.0003
Necrosis (vs absent)		
present	1.26 [0.98-1.63]	0.07

c



No. At Risk	0	1	2	3	4	5
STAS- & Nec-	227	185	150	120	85	68
STAS+ & Nec-	335	252	185	130	78	55
STAS- & Nec+	55	35	27	21	17	12
STAS+ & Nec+	95	60	42	25	14	7

Extended Data Fig. 10 | External validation of the impact of STAS and necrosis on disease-free survival. **a.** Summary of patient demographics and clinical characteristics of the Memorial Sloan Kettering Cancer Center cohort (n = 712 patients). **b.** Positivity of STAS and necrosis are incorporated with other tumour and clinical characteristics in a multivariable Cox proportional hazards model of

disease-free survival. **c.** Kaplan-Meier curve of disease-free survival, stratified by the positivity of STAS and the presence of necrosis (n = 712 patients). Hazard ratios were adjusted for age, pathological stage, smoking pack-years, surgery type, and receipt of adjuvant therapy. Numbers at risk are described at the bottom.